

Article

Sampling Uncertainties of Long-Term REMOTE-Sensing Suspended Sediments Monitoring over China's Seas: Impacts of Cloud Coverage and Sediment Variations

Liqiao Tian ¹, Xianghan Sun ¹, Jian Li ^{2,3,*}, Qianguo Xing ⁴ , Qingjun Song ⁵ and Ruqing Tong ¹

- ¹ State Key Laboratory of Information Engineering in Surveying, Mapping and Remote Sensing, Wuhan University, Wuhan 430079, China; tianliqiao@whu.edu.cn (L.T.); sunxh@whu.edu.cn (X.S.); tongruqing@whu.edu.cn (R.T.)
- ² School of Remote Sensing and Geomatics Engineering, Nanjing University of Information Science & Technology (NUIST), Nanjing 210044, China
- ³ State Key Laboratory of Simulation and Regulation of Water Cycle in River Basin, China Institute of Water Resources and Hydropower Research, Beijing 100038, China
- ⁴ Key Laboratory of Coastal Environmental Processes and Ecological Remediation, Yantai Institute of Coastal Zone Research, Chinese Academy of Sciences, Yantai 264003, China; qgxing@yic.ac.cn
- ⁵ Key Laboratory of Space Ocean Remote Sensing and Application, State Oceanic Administration, Beijing 10089, China; kingdream@mail.nsoas.org.cn
- * Correspondence: lijian@nuist.edu.cn; Tel.: +86-025-68778229

Received: 27 April 2020; Accepted: 11 June 2020; Published: 17 June 2020



Abstract: Satellite-based ocean color sensors have provided an unprecedentedly large amount of information on ocean, coastal and inland waters at varied spatial and temporal scales. However, observations are often adversely affected by cloud coverage and other poor weather conditions, like sun glint, and this influences the accuracy associated with long-term monitoring of water quality parameters. This study uses long-term (2013–2017) and high-frequency (eight observations per day) datasets from the Geostationary Ocean Color Imager (GOCI), the first geostationary ocean color satellite sensor, to quantify the cloud coverage over China's seas, the resultant interrupted observations in remote sensing, and their impacts on the retrieval of total suspended sediments (TSS). The monthly mean cloud coverage for the East China Sea (ECS), Bohai Sea (BS) and Yellow Sea (YS) were 62.6%, 67.3% and 69.9%, respectively. Uncertainties regarding the long-term retrieved TSS were affected by a combination of the effects of cloud coverage and TSS variations. The effects of the cloud coverage dominated at the monthly scale, with the mean normalized bias (P_{bias}) at 14.1% ($\pm 2.6\%$), 7.6% ($\pm 2.3\%$) and 12.2% ($\pm 4.3\%$) for TSS of the ECS, BS and YS, respectively. Cloud coverage-interfering observations with the Terra/Aqua MODIS systems were also estimated, with monthly P_{bias} ranging from 6.5% ($\pm 7.4\%$) to 20% ($\pm 13.1\%$) for TSS products, and resulted in a smaller data range and lower maximum to minimum ratio compared to the eight GOCI observations. Furthermore, with approximately 16.7% monthly variations being missed during the periods, significant “missing trends” effects were revealed in monthly TSS variations from Terra/Aqua MODIS. For the entire region and the Bohai Sea, the most appropriate timeframe for sampling ranges from 12:30 to 15:30, while this timeframe was narrowed to from 13:30 to 15:30 for observations in the East China Sea and the Yellow Sea. This research project evaluated the effects of cloud coverage and times for sampling on the remote sensing monitoring of ocean color constituents, which would suggest the most appropriate timeframe for ocean color sensor scans, as well as in situ data collection, and can provide design specification guidance for future satellite sensor systems.

Keywords: ocean color; remote sensing; sampling uncertainty; GOCI; Terra/Aqua MODIS; cloud coverage; suspended sediment

1. Introduction

Effective monitoring of water quality in coastal and open seas, including variations of phytoplankton levels, suspended sediments and colored dissolved organic matter, calls for uninterrupted sampling over appropriate time scales. Field survey-based water quality monitoring, using in-situ sampling, land or shipboard laboratory analysis, are precise but time- and labor-costly. Remote sensing data are favored for the advantages of rich spatial-temporal-spectral information. The benefits of remote sensing include its wider temporal and spatial range (coverage and scale) for water resource monitoring, and relatively low costs compared to the conventional field sampling approach [1,2]. Significant efforts have been made to applying remote sensing technologies to monitor water quality from local to global scales, and as a result, considerable progress has been achieved in our understanding of the behavior of coastal and inland waters [3–6].

Important ocean color sensors orbiting the earth include the Moderate Resolution Imaging Spectroradiometer (Terra/Aqua MODIS, 1999–present), the US Visible Infrared Imager Radiometer Suite (VIIRS, 2011–present), the Ocean and Land Color Instrument (Sentinel-3A OLCI, 2016–present) and the Korean Geostationary Ocean Color Imager (GOCI, 2010–present). Prepared to launch are several other ocean color sensors, including the Chinese HY-series satellites and NASA PACE mission [7,8]. Ideally, ocean color remote sensing unprecedentedly provides data for water quality properties at various spectral, temporal and spatial scales [9–11]. Unfortunately, applications of both in-situ and remote sensing methods are often limited by either low temporal or spatial resolutions, for regions that experience diurnal or semi-diurnal variations [12,13]. For instance, the spatial coverage or sampling frequency of traditional field sampling is often too small to derive meaningful conclusions [14,15]. The reliability of these methods is primarily determined by sampling protocol strategies with respect to sampling times and intervals. In most conditions, valid samplings are often limited: routine field surveys are generally conducted monthly by local authorities, such as the environmental or water quality agency. The most widely used Terra/Aqua MODIS satellites, designed to perform two observations a day, are particularly prone to disruption from cloud coverage and other poor weather conditions, as well as sun glints [16–18].

Although ocean color sensors, including the MODIS system, have been widely used for monitoring both short- and long-term water quality, previous studies have shown that observations are often hampered by cloud coverage, thick aerosol or sun glint [19]. As a result, it was found that each day, only 12%, on average, of the Aqua/MODIS ocean products were valid [10,19,20], and for some regions under persistent cloud coverage, monthly averaged valid observation could be less than one. High-latitude and equatorial oceans experienced the lowest levels of cloud-free period, with the valid number of observations being less than 2.4 per month [21]. Some research has been dedicated to improving temporal coverage for a single observation area by merging data from multiple satellite sources. For instance, observations merged from SeaWiFS and MODIS systems can produce valid data for up to 23% of the total ocean area, compared to approximately 18% from the MODIS system alone. Similar improvements can be derived by merging data over a four-day period, increasing the percentage of coverage to 30%–35% [22,23]. Despite efforts to improve the sampling frequency and coverage, the availability of valid observations from all the ocean color sensors remains limited.

These limitations greatly reduce the number of feasible applications of ocean color data, and can result in erroneous estimates of water quality indicators, such as mean Chl-a and suspended sediments levels. For coastal and open sea waters, where highly dynamic suspended sediment has been observed, high-frequency monitoring is required. Observations should preferably be taken every 30 min to 1 h [24], while inappropriate sampling frequencies and/or times could introduce large biases and

eventually lead to unscientific decisions in water management. Previous studies have indicated that inappropriate sampling time and frequency in water quality monitoring have led to statistical errors larger than 50% [7,25,26]. The facts of missing data from CZCS remote sensing resulted in a root mean-square error (RMSE) of 8% for annual mean chlorophyll concentrations, and a RMSE of 33% when determining the peak chlorophyll values [18]. For the Gulf of Mexico region, Barnes and Hu demonstrated that the difference in monthly mean Chl-a levels between MODIS and SeaWiFS datasets could be larger than 10% if monthly valid observations are fewer than 15 [27]. Despite these challenges and efforts to improve sampling strategies, systematic research on sampling coverage and its impacts on ocean color remote sensing data remains scarce.

For the aforementioned reasons, there is an urgent need to quantify the influence of cloud coverage in remote sensing and evaluate the impact of insufficient valid observations. Accordingly, appropriate sampling times for ocean color applications could be determined, and a benchmark for future satellite sensor planning be set. Pioneering research, using polar-orbit satellites like the MODIS system, showed that simulated datasets [18,25] with limited temporal coverage were inadequate for measuring diurnal variability. Thus, the geostationary-orbit (GEO) ocean color sensors have become prevalent to meet the demands of the high-frequency sampling of water quality. The first GEO ocean color satellite, the Geostationary Ocean Color Imager (GOCI), was launched by South Korea in 2010, and takes hourly measurements during the daytime [16]. GEO satellites, including GOCI, provide high-frequency sampling to capture the dynamic of coastal/inland waters [28]. GEO data have been widely used in ocean color remote sensing applications, for monitoring parameters such as the chlorophyll, suspended sediment and colored dissolved organic matter concentrations [29–31]. Most commonly, studies on the remote sensing of water quality involve time-series analysis of, for example, TSS in the regions of interest. Therefore, a fundamental question is how these sampling uncertainties revealed above would affect the estimations of long-term trends in TSS observations. The differences among these time-series TSS data were examined to answer the following questions: do they show the same magnitudes of mean monthly TSS? Do they show the same seasonality (i.e., monthly maximum/monthly mean ratio)? Do they show the same inter-annual changes and long-term trends?

By using the long-term high-frequency GOCI datasets for the China seas, this study aimed, firstly, to quantify cloud coverage over targeted waters at long-term scales, and secondly, to provide a solution to resolve the effects of sampling times on the remote sensing monitoring of total suspended sediment (TSS) in highly dynamic waters. Thirdly, the level of uncertainty in the data produced by the satellite sensors most commonly used for ocean color observations, the Terra/Aqua and MODIS systems, in ocean color remote sensing were assessed, thus providing a benchmark for the development of sampling strategies.

2. Material and Methods

2.1. Study Areas and GOCI Data

GOCI is the first geostationary ocean color satellite sensor, onboard the South Korean Communication, Ocean and Meteorological Satellite (COMS). It has successfully collected data covering geographical regions between 110°E and 150°E, and 2°N and 50°N, with a 500-m spatial resolution, since its launch in June 2010 [16,32]. GOCI was designed to measure six visible light bands (at 412, 443, 490, 555, 660 and 680 nm) and two near infrared bands (at 745 and 865 nm) with hourly observations during the daytime. GOCI aims to monitor the marine environment in real time with a rapid data-acquisition rate [33]. More than two-thirds of the coastal and sea waters within the Chinese maritime territory are imaged hourly by GOCI, which greatly increases the sampling frequency of China's seas.

Figure 1 shows a red-green-blue (RGB) composite image from GOCI acquired on May 13, 2017, covering the China seas, including the Bohai Sea (BS), the Yellow Sea (YS) and the East China Sea (ECS), when there was massive cloud coverage across the region. The Bohai Sea is a semi-enclosed sea located

in the northeastern region of China, with an area of approximately 7700 km² and an average water depth of 18 m, extending 550 km from south to north and 300 km from west to east [34]. The Bohai Sea is dominated by an irregular semi-diurnal tide. The constituent of surface sediment is mainly silt and clayey silt, and the spatial variations of suspended sediment in the Bohai Sea was dominated by the river input, together with coastal resuspension caused by hydrodynamics [35,36]. The Yellow Sea flows to the Bohai Sea through the narrow Bohai straight in the east. The Yellow Sea has an area of approximately 380,000 km² with average depth of about 44 m [37]. In recent decades, abundant sediments were exported to the Bohai and Yellow Sea, caused by human activities together with the accumulative effects of winds, currents and the resuspension of particles [38]. Previous research showed that wind and tide are the principal agents for sediment resuspension [39,40]. The East China Sea is connected to the Yellow Sea at the north, with a continental shelf of approximately 640 km and an average water depth of 72 m [41]. This wide and shallow shelf receives a great amount of sediment from the Yangtze river, one of the largest rivers in the world. The annual sediment load from the Yangtze River is about 480 million tons [42].

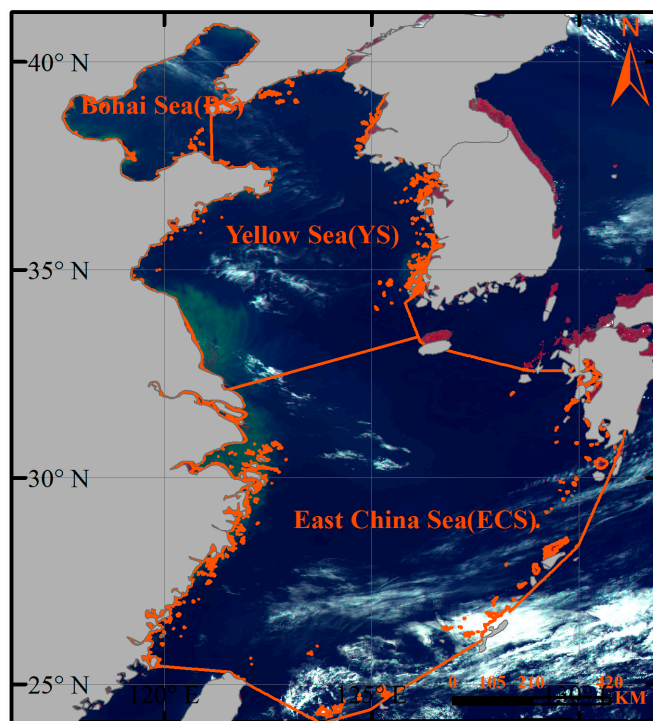


Figure 1. Map of the study area. The red–green–blue (RGB) image shows observations from the Geostationary Ocean Color Imager (GOCI) on 13 May, 2017.

GOCI obtains eight hourly measurements during daytime from 08:30 to 15:30 local time and provides unparalleled high-frequency data for close monitoring of the highly dynamic aquatic environment [43]. The GOCI L1B data products were downloaded from the website (<http://kosc.kiost.ac.kr/eng/>). High-frequency observations from 2013 to 2017, 17,120 images in total, were obtained to analyze the cloud coverage, interrupting and reducing frequency of valid samplings, and to analyze the associated uncertainty levels. Note that although GOCI data were evenly selected from different months, the averaged valid observations varied monthly, as listed in Table 1 for each sub-region. The valid pixels in each image were first determined using “Cloud or Ice” flags provided along with the GOCI products. Then the valid observations (%) for each month were calculated for each pixel as the ratio of the valid number of data to total images of the month. In general, more valid observations were available in summer than in winter for the East China Sea, but opposite trends were observed for the Bohai Sea and the Yellow Sea, with more valid data in winter.

Table 1. Monthly averaged valid observations (%) of GOCI data from 2013 to 2017.

| | East China Sea (ECS) | Bohai Sea (BS) | Yellow Sea (YS) |
|-----------|----------------------|----------------|-----------------|
| January | 29.21 | 56.52 | 40.64 |
| February | 16.76 | 50.81 | 29.11 |
| March | 20.15 | 34.07 | 25.59 |
| April | 31.05 | 26.98 | 19.63 |
| May | 45.01 | 28.66 | 32.25 |
| June | 48.04 | 20.60 | 19.22 |
| July | 67.47 | 13.63 | 18.30 |
| August | 51.78 | 24.19 | 30.87 |
| September | 39.78 | 24.60 | 30.84 |
| October | 36.44 | 26.78 | 36.74 |
| November | 44.86 | 52.26 | 52.12 |
| December | 29.79 | 62.70 | 46.36 |

2.2. Data Processing

GOCI Level-1 datasets containing calibrated-at-sensor radiance measurements were batch-processed using a module of the GOCI Data Processing System (GDPS) software package version 1.4.1 (released in December 2015) to generate spectral remote sensing reflectance (RRS) images. Atmospheric correction of the GOCI datasets was performed using an atmospheric correction algorithm similar to that used with the MODIS system. Details of the atmospheric correction scheme used with the GDPS software have already been published [44,45].

After atmospheric correction, two TSS algorithms were applied: the YOC algorithm and the Case-2 algorithm, to obtain the required TSS data products. The YOC algorithm [46] is an algorithm developed for the region and validated with extensive in situ measurements collected in the areas covered by GOCI, including the East China Sea and the Yellow Sea. For extremely turbid water (e.g., the estuarine part of the Yangtze River and the coastal area of the Yellow Sea, where TSS > 100 g/m³), the YOC algorithm does not perform well. For this reason, the new Case-2 algorithm for turbid water was developed using in situ datasets obtained from the western coastal area of the Korean Peninsula [46,47]. Validation of the standard GOCI data products was carried out for both low and highly turbid waters, including the Bohai Sea, the Yellow Sea and the East China Sea [43,48–51]. These studies showed that the GOCI ocean color data products are in close agreement with data from the MODIS and MERIS systems and are effective for monitoring water quality in these regions.

Cloud mask products derived using GDPS was used to analyze the cloud coverage in the target regions at both short- and long-term temporal scales. The algorithm for cloud masking is a threshold-based method using atmospheric corrected images. The sum of multiply scattered aerosol reflectance (ρ_a) and interactively scattered reflectance between aerosols and molecular (ρ_{ra}), was used as $[\rho_a(865\text{nm}) + \rho_{ra}(865\text{nm})]$, to determine whether a pixel is cloud or not. The default value of the threshold is 0.028 Sr⁻¹, and thus pixels with $[\rho_a(865\text{nm}) + \rho_{ra}(865\text{nm})]$ larger than 0.028 were defined as cloud pixels. To account for band registration errors or cloud movements, neighboring pixels were also masked [52].

2.3. Cloud Coverage and Total Suspended Sediment Uncertainties Analysis

- (1) Cloud statistics: Monthly cloud coverage percentage (CCP) was first calculated for each pixel from five years of GOCI cloud mask data using the ratio of cloud coverage to the total numbers of observations. The spatial and temporal trends of monthly CCP were then obtained.
- (2) Estimation of TSS uncertainties: The mean normalized bias (P_{bias}) of TSS observations due to insufficient sampling rates was estimated using the statistical average of the absolute (unsigned) percentile differences between single observations at each hour h and the daily mean TSS from

eight observations. Note that P_{bias} were only calculated for pixels that satisfy eight valid coverages per day. The value of P_{bias} was calculated through the following equation:

$$P_{bias} = \frac{1}{N} \sum_{i=1}^N \left| \frac{\text{TSS}(h)_i - \text{TSS}(\text{ave})_i}{\text{TSS}(\text{ave})_i} \right| \times 100 \quad (1)$$

where N is the number of valid observations for each pixel from 2013 to 2017, and $\text{TSS}(\text{ave})_i$ is the bias for the i th day observation:

$$\text{TSS}(\text{ave})_i = \sum_{h=1}^8 \text{TSS}(h)_i / 8 \quad (2)$$

Similar indexes have also been used in previous studies to estimate the sampling bias of different satellite observations [18,25]. During the statistical evaluation of each day's results, pixels that returned fewer than 8 valid observations were neglected. The monthly and annual mean biases for TSS observations were then obtained by averaging the hourly bias over the month and the year.

2.4. Sensitivity Analysis of TSS Sampling Uncertainties

Two factors, cloud coverage and TSS variations, were assumed to influence the sampling bias of TSS in highly dynamic waters, and were quantified by coefficient of variation (CV = Standard Deviation/Mean) of each pixel across the entire time-series. An hourly or monthly CV grid was created by stacking all the TSS images per hour or month, and by calculating statistics for the entire image array with a CV value for each pixel. For a specific hour or month, the CV could be calculated as follows:

$$CV = \frac{\sqrt{\frac{1}{N} \sum_{i=1}^{i=n} (\text{TSS}_i - \overline{\text{TSS}}_i)^2}}{\overline{\text{TSS}}} \quad (3)$$

where TSS_i is the TSS of the i th observation, $\overline{\text{TSS}}$ is the average TSS for the study period, and N is the total number of observations. Larger CV values indicate that the data are more dispersed and TSS variability is greater over time, whereas smaller CV values mean that the data are more consistent and the TSS are more stable.

To analyze the effect of one factor within the influence of multiple factors, composite effects should be removed during the correlation analysis. The Partial Correlation analysis is an effective method for investigating the relationships between TSS bias and influencing factors, including cloud coverage and TSS variations. In addition, the P value (probability associated with significance) was used to test the significance of the correlations, where a P value < 0.05 is regarded as a significant correlation. The specific formula of partial correlation coefficient is as follows:

$$r_{xy} = \frac{\sum_{i=1}^N (x_i - \bar{x})(y_i - \bar{y})}{\sqrt{\sum_{i=1}^N (x_i - \bar{x})^2 (y_i - \bar{y})^2}}, \quad (4)$$

$$R_{xy,z} = \frac{r_{xy} - r_{xz}r_{yz}}{\sqrt{(1 - r_{xz}^2)(1 - r_{yz}^2)}}, \quad (5)$$

where r_{xy} is the Pearson correlation coefficient of variables x and y , x_i is the TSS bias value of the i th observation, and y_i is the cloud coverage or the CV of the i th observation. \bar{x} and \bar{y} are the mean values of the corresponding variables. $R_{xy,z}$ is the Partial correlation coefficient between x and y , with the effects of z removed.

3. Results

3.1. Cloud Coverage

The spatial distribution and the temporal trend of monthly cloud coverage percentage (CCP) are shown in Figures 2 and 3. The studied areas demonstrated significant intra-annual variabilities in CCP, both spatially (Figure 2) and temporally (Figure 3). Averaged monthly CCP of the whole study area peaked in March at approximately 77.1%, decreased to the lowest level in July at approximately 52.3%, and then increased again to approximately 72.2% in November. This is consistent with previous results obtained by Xiao et al. [20], based on merged imagery of daily observations from the SeaWiFS, MODIS, MERIS and VIIRS systems. Obvious monthly CCP patterns were identified for sub-regions of the BS, the YS and the ECS area. The BS and YS areas had similar temporal patterns, with peak CCP in July and lower CCP in December, while an opposite pattern was shown in the ECS region, with low CCP in July and high CCP in December.

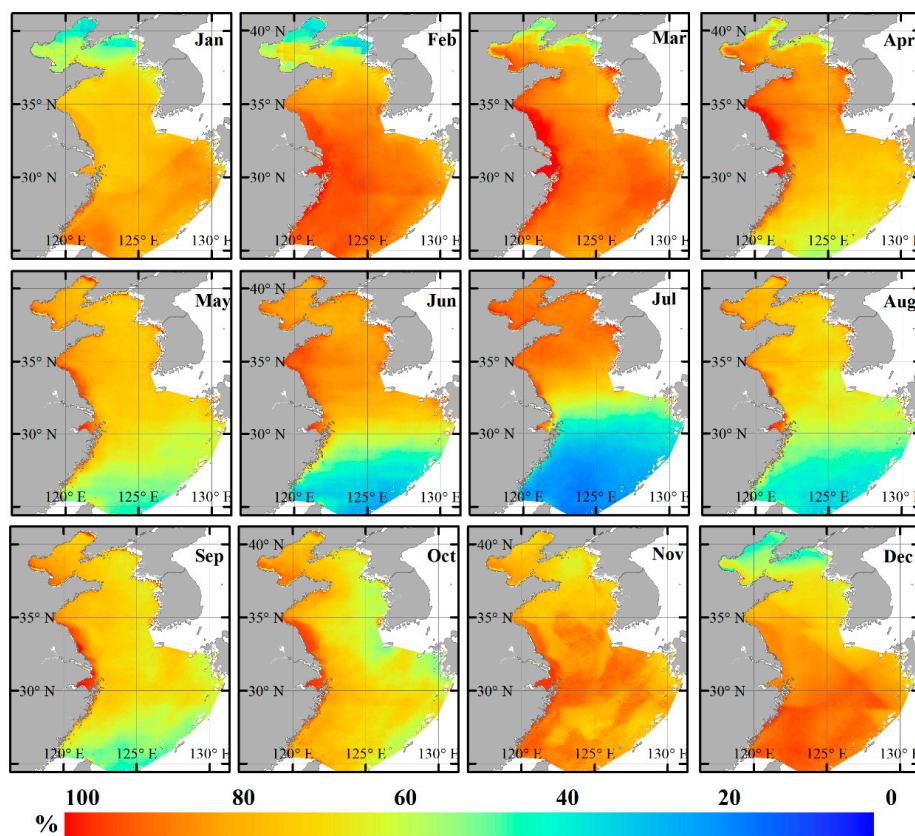


Figure 2. Monthly cloud coverage percentages for China's seas from GOCI observations between 2013 and 2017.

The extremely high CCP for the China seas indicates that large portions of the observations from remote-sensing satellites are blinded by clouds. To substantiate this point, the lowest monthly CCP averages for the ECS, BS and YS were found to be 32.5%, 37.3% and 47.9%, equivalently reducing the number of days of cloud-free observations to 20.1, 18.6 and 16, respectively. In the months of the highest CCP, there were only 5, 4 and 5.7 cloud-free days for the ECS, BH and YS area, respectively. The average CCP (standard deviation) values were 62.6% (14.1%), 67.3% (15.5%) and 69.9% (8.6%) for the ECS, BS YS areas, respectively, and it was 65.7% (7.7%) for the whole area. Therefore, it is imperative to understand the effects of the cloud coverage on the remote sensing of TSS in these highly dynamic waters, and to assess the uncertainties in the observations from data from the Terra/Aqua MODI satellite, the most commonly used satellite sensors.

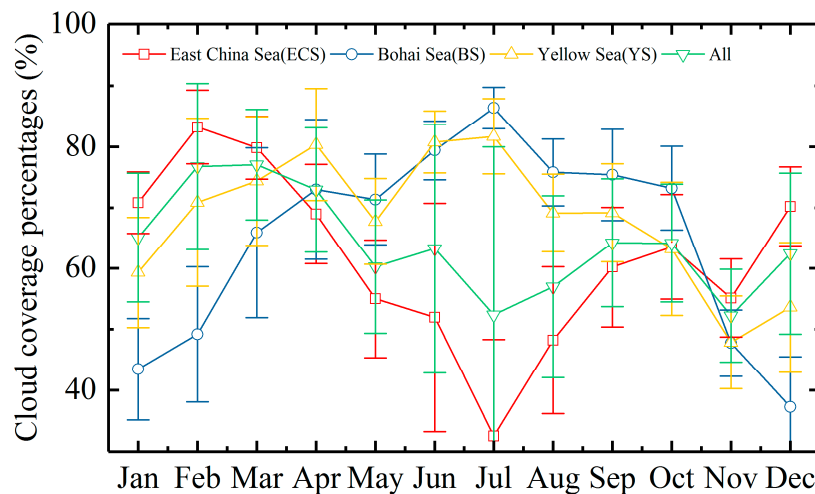


Figure 3. Cloud coverage percentages by month for China's seas from GOCI observations between 2013 and 2017.

3.2. Biases of TSS Observations

The spatial distribution map of hourly TSS biases was calculated and is presented in Figure 4, while the statistical results representing the temporal trends for the different regions are illustrated in Figure 5. TSS bias is the same as P_{bias} in the following text of the paper. Notable spatial and temporal variations were revealed throughout the Chinese seas. The average (by standard deviation) biases for hourly TSS estimates were 12.8% (2.7%), 7.0% (1.7%), 10.2% (2.3%) and 11.5% (2.5%), in the ECS, BS, YS, and the whole study area, respectively. The results revealed that the maximum TSS bias was as much as 18.3%, 9.8%, 14.5% and 16.5% for the aforementioned sea regions. The largest TSS bias was found in the ECS, while the smallest TSS bias occurred in the BS. The diurnal variation of TSS bias in the whole area shows a decreasing trend from morning, at around 08:30, to the early afternoon, around 13:30 local time. During this period the bias decreased from 13.3% to 8.9%. It then increased to 16.5% at 15:30. Similar diurnal trends were also observed in the ECS, BS and YS.

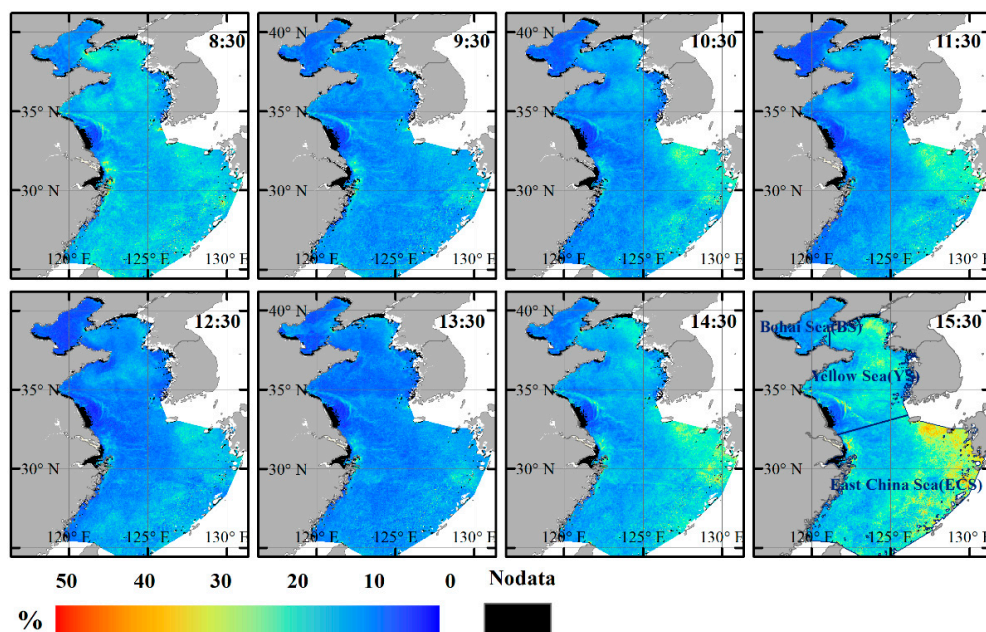


Figure 4. Hourly TSS bias in Chinese seas from GOCI observations from 2013 to 2017.

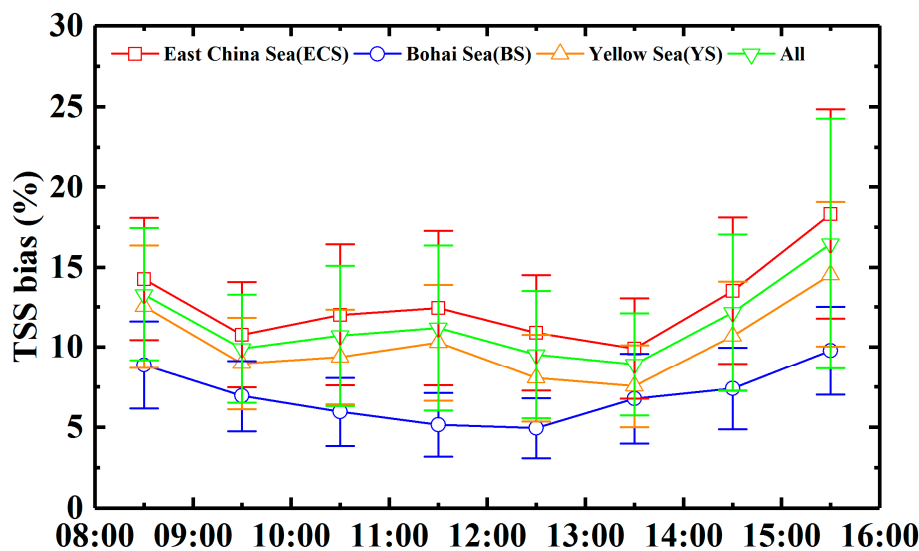


Figure 5. Temporal trends of hourly TSS bias of Chinese seas from GOCI observations.

The spatial distributions and temporal trends of the monthly bias for TSS are shown in Figures 6 and 7. The pixels that did not satisfy the criterion of eight valid observations a day were labeled as “Nodata” (black color in Figure 6) during the statistical analysis. In general, the average monthly bias (\pm standard deviation) for the TSS was 14.1% (\pm 2.6%), 7.6% (\pm 2.3%) and 12.2% (\pm 4.3%) for the ECS, BS and YS areas respectively, and was 12.8% (\pm 2.7%) for the whole study area.

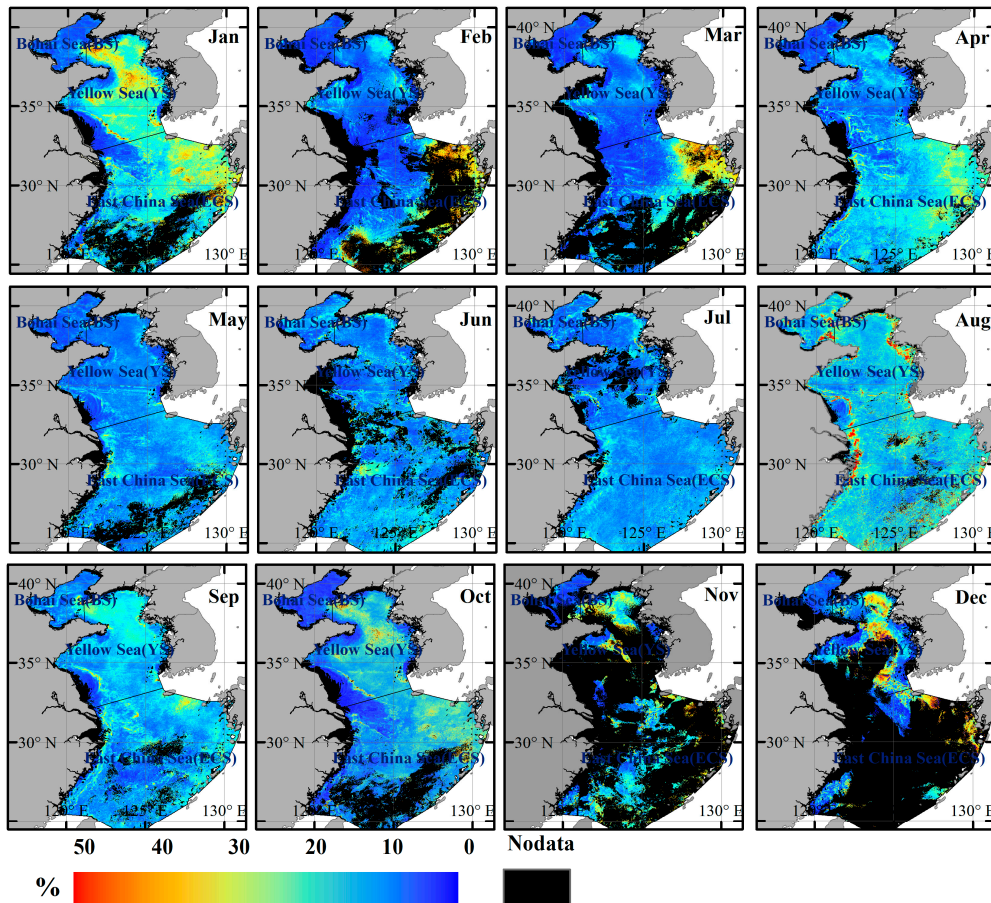


Figure 6. Monthly bias for total suspended sediments (TSS) in China's seas from GOCI observations from 2013 to 2017.

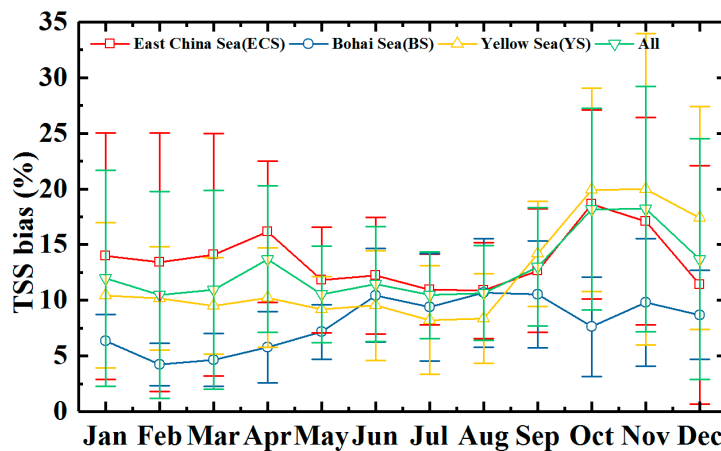


Figure 7. Changes of monthly bias for TSS in China's seas from GOCI observations.

The maximum monthly bias for TSS was 18.6% and 19.9%, for the ECS and YS in October, and so too was the maximum monthly bias for the whole study area, at 18.2% in October. The maximum monthly bias was 10.7% for the BS region in August. Among the three areas, the YS area had the largest while the BS area had the smallest monthly bias for TSS, and the BS area also showed a smaller overall monthly biases than the other two area.

The changes in monthly bias of TTS, in the ECS and YS, to some extent mirrored that of the whole studied area, with relatively lower biases from May to August, and relatively higher ones from October to December. In comparison, the monthly TSS bias for the BS region displayed almost a reversed pattern, with relatively higher values from June to September, and relatively lower values from October to December and from January to April.

The spatio-temporal variations in monthly TSS biases arise in a manner agreeable with that of the cloud coverage percentage (Figures 2, 3, 6 and 7). Lower bias values coincided, both temporally and spatially, with higher cloud coverage percentage, and vice versa. For areas with extremely high cloud coverage, such as the majority of the ECS in November and December and the coastal areas of the YS from January to July (Figure 2), the bias for TSS cannot be calculated due to a lack of valid observations ("Nodata" area in Figure 6). Consistently, the monthly CCP (the probability of cloud coverage) for these areas in the corresponding months (Figure 2) was higher than 90%. The changes of monthly TSS bias for the YS area, however, could not be entirely attributed to the cloud coverage over this area, because the changes of monthly biases for TTS did not correlate with the changes of the monthly CCP all year around (Figures 3 and 5).

3.3. Factors Affecting TSS Sampling Uncertainties

Two factors were assumed to potentially influence the uncertainties of retrieved TSS values. The first one is the natural variation of TSS itself, as results would be more susceptible to sampling times and frequencies in waters with highly dynamic TSS. In waters with stable TSS, different sampling times and frequencies make no difference to the TSS estimates. In this study, variations of TSS were indicated using the coefficient of variation (CV) to normalize variations across the whole study region, including both highly turbid and relatively clear waters. The second factor is the cloud coverage, which affects the number of valid observations, and thus affects the variations of obtained TSS values over both the short and long term.

The hourly and monthly trends of TSS CVs across the study areas are presented in Figures 8–11. Significant spatial variations were revealed in the regions of concern at both hourly and monthly scales. At the hourly scale, larger CVs were calculated for offshore waters along the East China Sea (Figure 8), and the coastal zones of the Bohai and Yellow seas indicated higher temporal variations of TSS levels in these areas; they are dominated by tidal currents that control the sediment transport and resuspension [51,53]. Regions with higher TSS bias also displayed larger CVs, which indicates that

most of the hourly TSS bias may be due to the TSS variations (Figure 9). Overall, the temporal trends in the TSS CVs in each subregion were similar to those of the TSS bias, which decreased from morning, around 08:30, to around 13:30 local time, and then increased until 15:30, with the trough found at around 13:30. The magnitudes of the TSS CVs were also consistent with the magnitudes of the TSS bias for the subregions. More specifically, the East China Sea generated the largest TSS bias and CV values, followed by the Yellow Sea. The lowest TSS bias and CV levels were found in the Bohai Sea.

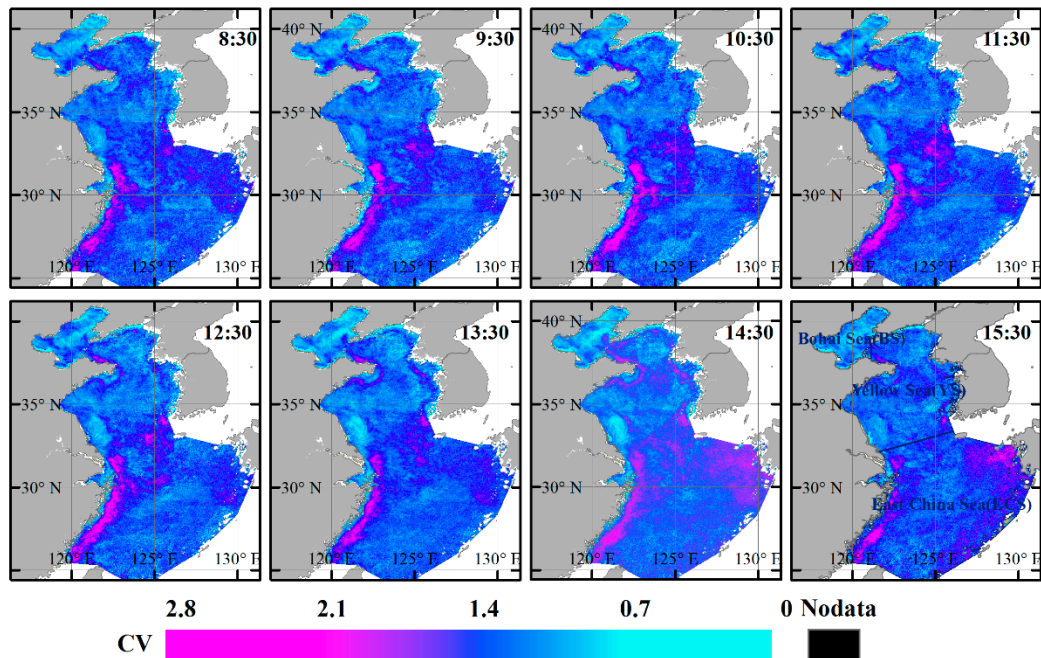


Figure 8. CV in hourly TSS levels in Chinese seas from GOCI observations from 2013 to 2017.

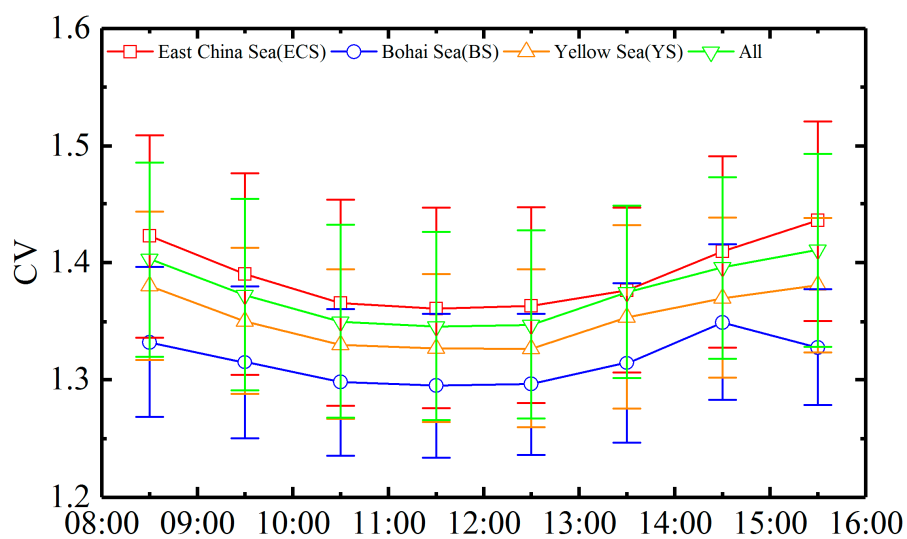


Figure 9. CV trend in hourly TSS levels in Chinese seas from GOCI observations from 2013 to 2017.

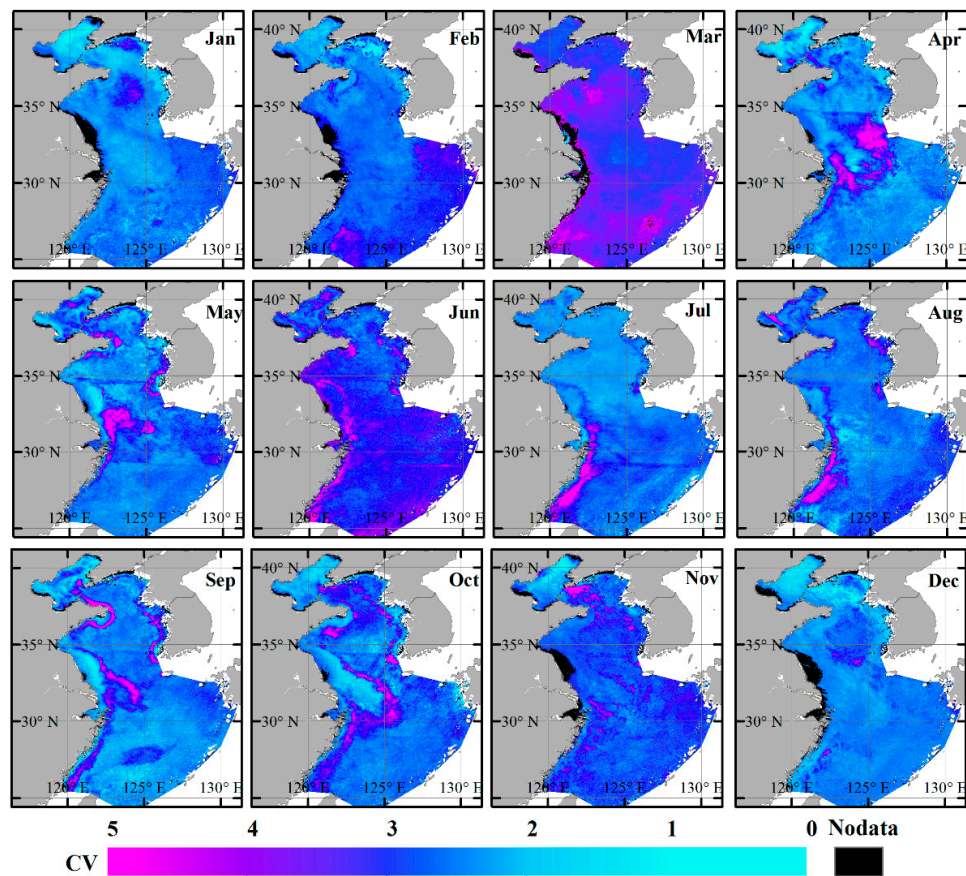


Figure 10. CV for monthly TSS levels in China's seas from GOCCI observations from 2013 to 2017.

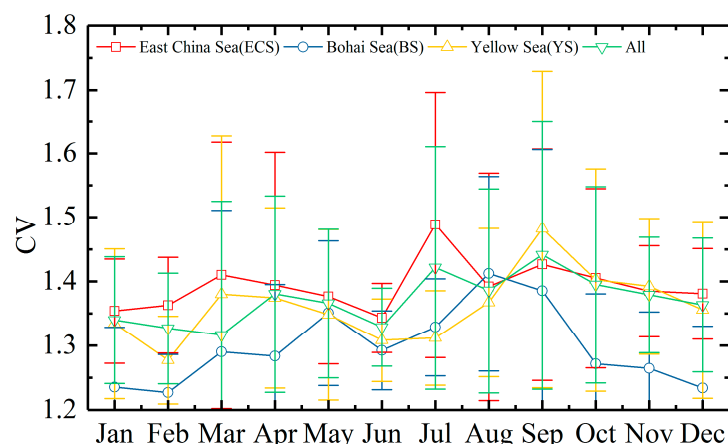


Figure 11. Changes of coefficient of variation (CV) of monthly TSS levels for China's seas from GOCCI observations from 2013 to 2017.

The monthly TSS CV values showed notable spatial and temporal variations (Figures 10 and 11). Since CV was determined as the ratio of standard deviation to mean value, areas that experienced high dynamic TSS variations would have higher CV values. Larger CV values were observed along the shorelines of the Yellow Sea and the East China Sea during the summer and autumn seasons, induced by river inflow in the rainy season, whereas the winter season displayed lower CVs. There are evident plumes where the CV differs from surrounding areas, between the coastal regions and the open oceans, which may have been caused by sediment resuspension driven by the combined effects of river discharges, winds, currents and waves in these zones [54]. Previous studies have demonstrated that

suspended matter levels increased significantly from the coastal zones to the open oceans, which were blocked by the warm Taiwan and Kuroshio currents [55,56].

The monthly biases and CVs for TSS did not support the hypothesis that the sampling bias was significantly affected by the TSS variations on a monthly scale for the entire study area. Areas with larger biases did not necessarily coincide with higher CV values, and the changing temporal patterns of the two parameters were not consistent either. These results demonstrate that the monthly observations of TSS levels are not solely determined by the TSS variations. Coastal regions with higher CVs were, however, prone to have larger TSS biases.

The results above suggests that both cloud coverage and TSS variations contributed to the TSS sampling biases, spatially and temporally, which indicate that areas with higher cloud coverage or TSS variation are prone to having greater sampling biases. For instance, the TSS biases of the Yellow Sea and East China sea in November, December and January were higher than in other months, which were consistent with the temporal trends of cloud coverages in these areas. But for the Bohai Sea, higher TSS biases were revealed in the summer, and lower ones revealed in the winter, and these coincident with cloud coverage trends in the area. Thus, the sensitivity of the sampling biases to the two factors should be further analyzed.

Maps of the partial correlation of TSS sampling bias with cloud coverage and with TSS CV were obtained at monthly scales, each month using 60 matchups. A correlation greater than 0.6 or 0.8 is generally described as a high or strong correlation, whereas a correlation less than 0.6 is generally described as a weak correlation.

Figure 12 shows the correlations between the hourly TSS sampling biases and the cloud coverage (Figure 12a) and the TSS CVs (Figure 12b), together with the *P* value maps (Figure 12c,d). In general, the correlation between the TSS sampling biases and variations was revealed to be higher than that for the relationship between sampling biases and the cloud coverage, at the hourly scale. The results are consistent with the analysis in Sections 3.2 and 4.1, which indicated that the spatial and temporal patterns of hourly scale TSS sampling biases are more closely correlated with the TSS variations than with cloud coverage.

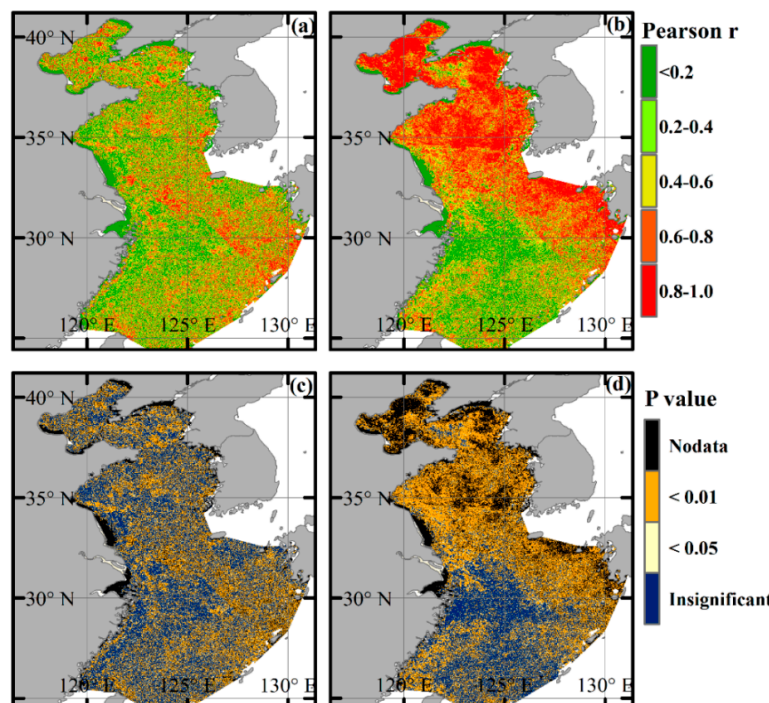


Figure 12. Partial correlation coefficients (*P* value) of TSS biases with cloud coverage (a,c), and TSS biases with TSS CV (b,d) at the hourly scale.

A strong correlation between sampling biases and TSS CVs was found in the Bohai Sea, Yellow Sea, and the northeastern section of the East China Sea, while the rest of the ECS showed a lower correlation, of less than 0.6. A total of 61.6% of the total study area was significantly affected ($P < 0.05$) by the TSS variations, while 47.6% was significantly affected by the cloud coverage. Table 2 presents the area statistics for correlation, and P values for each subregion. The results clearly showed that the TSS sampling bias is more sensitive to TSS variation than to cloud coverage, for hourly scale observations. For instance, observations for approximately 87% of the Bohai Sea and 86% of the Yellow Sea were significantly affected by the TSS variations. On the contrary, 48.4% and 46.9% of these two subregions were significantly affected by cloud coverage. About half of the area of the East China sea was significantly affected by the TSS variations.

Table 2. Area percentage statistics: P value for each subregion at the hourly scale.

| | P Value | Bohai | East China Sea | Yellow Sea | All |
|---------------|----------------|--------------|-----------------------|-------------------|------------|
| Cloud impacts | $P < 0.01$ | 35.20% | 34.60% | 33.50% | 34.30% |
| | $P < 0.05$ | 48.40% | 47.80% | 46.90% | 47.60% |
| CV impacts | $P < 0.01$ | 79.80% | 37.80% | 77.90% | 50.20% |
| | $P < 0.05$ | 86.90% | 50.60% | 86.10% | 61.60% |

Figure 13 presents maps of correlation for P values between the monthly bias and the cloud coverage (Figure 13a,c), and between monthly bias and the TSS CV (Figure 13b,d). Both the cloud coverage and the TSS variations obviously generated uncertainties in obtaining TSS. For partial areas of the Bohai Gulf, the central Yellow Sea, and the southeastern area of the East China Sea, amounting to 17.1% of the studied areas, sampling bias strongly correlated with cloud coverage. In total, approximately 51.4% of the entire studied region had correlation coefficients higher than 0.6. Areas where TSS variations correlated more closely with sampling biases were found along the coastal regions and in the southeastern area of the East China Sea.

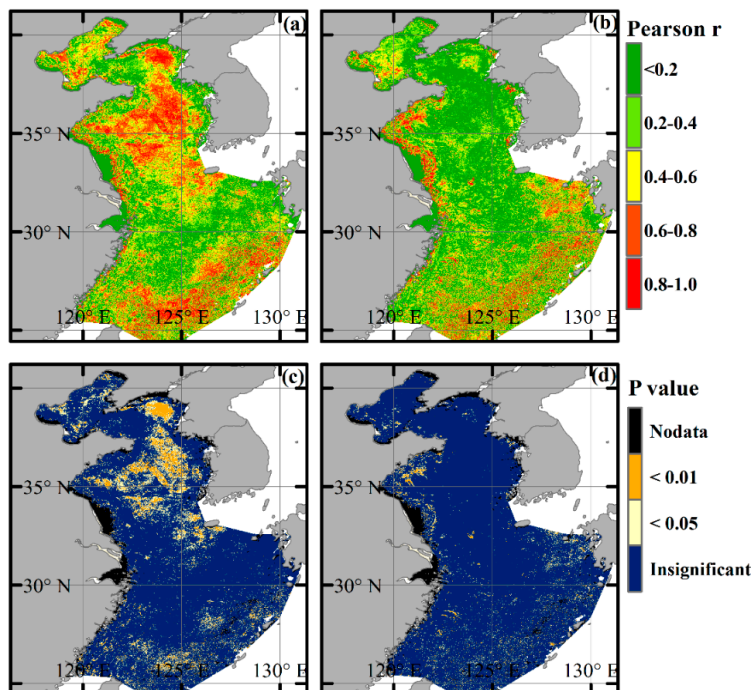


Figure 13. Partial correlation coefficients (P value) of TSS biases with cloud coverage (a,c), and TSS biases with TSS CV (b,d) at the monthly scale.

Secondly, the impact of the cloud coverage on sampling biases overshadows that of the TSS variations for monthly observations. At the $P < 0.05$ level, 17.6%, 10.9% and 29.5% of the TSS observations in the Bohai Sea, the East China Sea and the Yellow Sea were significantly affected by cloud coverage, respectively, while 4.4%, 6.9% and 4.5% of these seas, in respective order, were significantly affected by TSS variations (Table 3). It is worth noting that more than 50% of the observations displayed correlation coefficients larger than 0.4 for either cloud coverage or TSS variations. For example, 55% and 60% of the TSS observations in the East China Sea showed P values greater than 0.4, for cloud coverage and TSS variations, respectively.

Table 3. Area percentage statistics: P values for each subregion at the monthly scale.

| | P Value | Bohai | East China Sea | Yellow Sea | All |
|---------------|----------------|--------------|-----------------------|-------------------|------------|
| Cloud impacts | $P < 0.01$ | 3.50% | 2.90% | 10.90% | 5.50% |
| | $P < 0.05$ | 17.60% | 10.90% | 29.50% | 17.10% |
| CV impacts | $P < 0.01$ | 0.90% | 1.90% | 1.60% | 1.70% |
| | $P < 0.05$ | 4.40% | 6.90% | 4.50% | 5.80% |

3.4. Impacts of Sampling Strategy on Long-Term TSS Trends Monitoring

Time-series of remote sensing data are commonly used for long-term water quality estimations in the regions of interest. Therefore, the impacts of cloud coverage and sampling frequency on sampling uncertainties associated with long-term trends in TSS observations should be resolved. The differences among the TSS time-series retrieved from different satellite sources were examined to determine whether they are consistent regarding the magnitude, seasonality, inter-annual changes and long-term trends, for monthly TSS. To address this, monthly and annual TSS statistics from Terra/MODIS (“simulated” using GOCI 11:30 AM images), Aqua/MODIS (GOCI 13:30 PM images) and Terra/Aqua MODIS (combined observations using GOCI 11:30 and 13:30 images) observations were analyzed and compared to the eight observations of GOCI as references.

Figure 14 provides the climatology monthly maps of GOCI-observed TSS from 2013 to 2017. The TSS concentrations are higher along the coasts, especially in the Bohai Sea and the Yangtze River estuary, while being lower in the middle of the Yellow Sea and the southeastern area of the East China Sea. From January to March, and October to December, significantly high TSS values ($>\sim 10 \text{ g/m}^3$) are observed in most regions of the study area, excluding the middle of the Yellow Sea and the southeastern area of the East China Sea. In general, TSS values are lowest in summer months (July to August), and increase in autumn and winter. These seasonal patterns are consistent with findings in Yuan et al. (2008), whereby the most turbid plumes were observed during winter, and decreased in the following spring and through summer [57].

Figure 15 presents the changes of monthly mean TSS from 2013 to 2017, retrieved from GOCI, Terra/MODIS, Aqua/MODIS and Terra/Aqua, for the entire study regions (ALL) and each subregion (ECS, YS, BS). In addition, the first derivative, the instant slope of the tangent line of the TSS-time curve, is presented. In this study, we defined “missed trends” to quantitatively compare the accuracy of different sensors in capturing long-term monthly variations of TSS. First, the baselines of monthly TSS trends were determined using GOCI observations, and the trend between each two months was calculated as the first derivative. A positive derivative signifies an increasing trend, and a negative derivative signifies a decreasing trend, of TSS between each month. Then, the monthly TSS trends from Terra/Aqua MODIS were also calculated and compared to the GOCI results. If the trends observed from GOCI and Terra/Aqua MODIS were opposing, then the numbers of missed trends were added. This process was checked for all months, and the total numbers of missed trends were obtained. Despite the analogous seasonal pattern, significant difference existed in these time-series of monthly TSS.

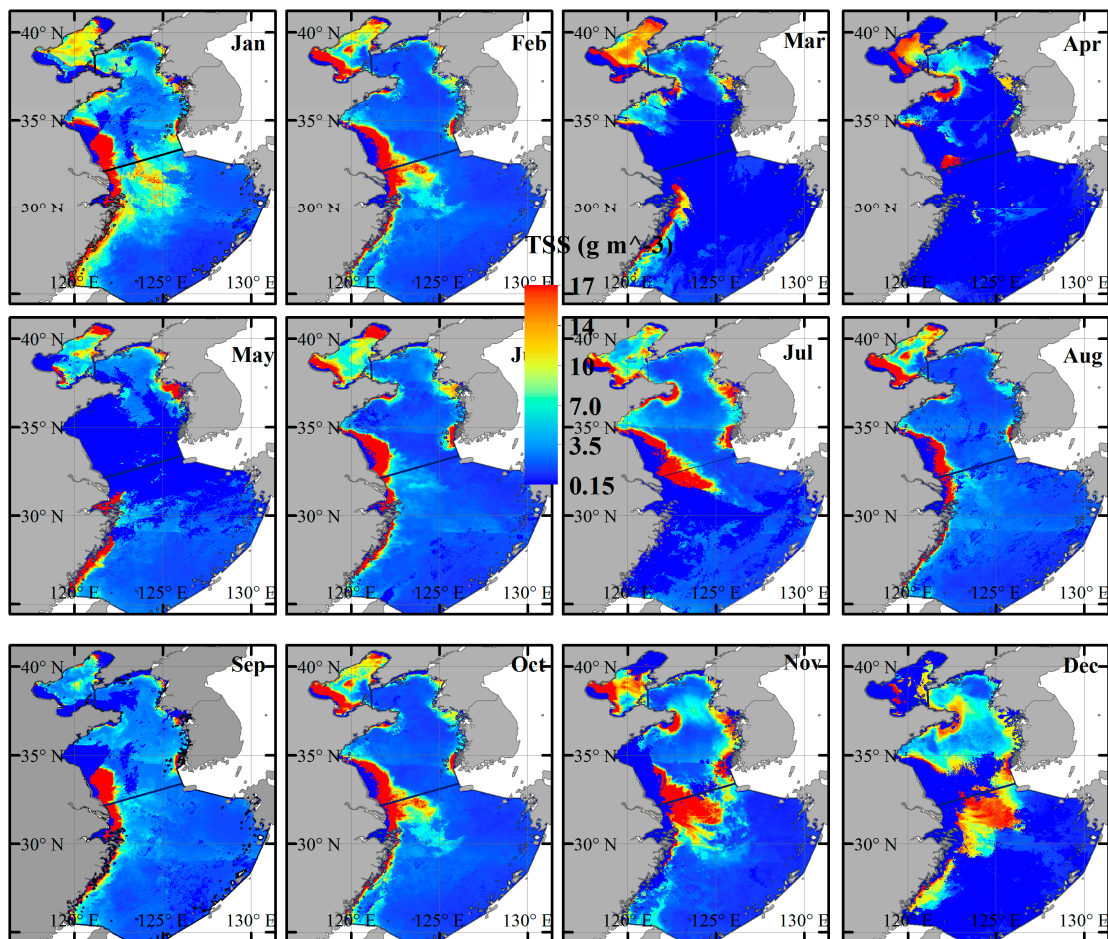


Figure 14. Monthly averaged TSS images using GOCI observations from 2013 to 2017.

Specifically, for the whole region, ECS, YS and BS, the ranges of monthly mean TSS obtained from eight GOCI observations were larger than those obtained from one Terra or Aqua/MODIS observation, as well as those from two Terra/Aqua combined observations. For the entire study region, GOCI observations showed a range of 4.47 g/m^3 (with the maximum and minimum TSS of 1.35 and 5.52 g/m^3), whereas the ranges were 2.96 , 2.84 and 2.65 g/m^3 for Terra, Aqua and Terra/Aqua MODIS, respectively, as shown in Table 4. Similar differences were also observed in subregions of the ECS, YS and BS. This inconsistency indicates that single, or a limited number of, observations would miss information on variations of TSS during long-term monitoring, as substantiated by the smaller maximum to minimum ratios in comparison with the eight GOCI observations, as listed in Table 4. For extremely dynamic waters, as in the ECS [58], the maximum to minimum ratio obtained from GOCI was 16.57 , almost five times larger than that for the single daily Terra or Aqua/MODIS observations. The effects of missing information, due to insufficient sampling frequency, on annual TSS variations were also observed, as shown in Figures 16 and 17. Larger variations indicated by standard deviation (STD) and CV were revealed from GOCI data, despite similar temporal trends and spatial distributions, compared to Terra/Aqua MODIS data. The higher CV from GOCI observations means more detailed TSS variations were observed from high-frequency remote sensing data. For instance, with eight observations a day, GOCI is able to capture TSS variations within each day, from 8:30 to 15:30, which Terra/Aqua MODIS would have missed. Moreover, the single or combined Terra and Aqua/MODIS seemed to overestimate annual trends of TSS for the entire areas and each subregion.

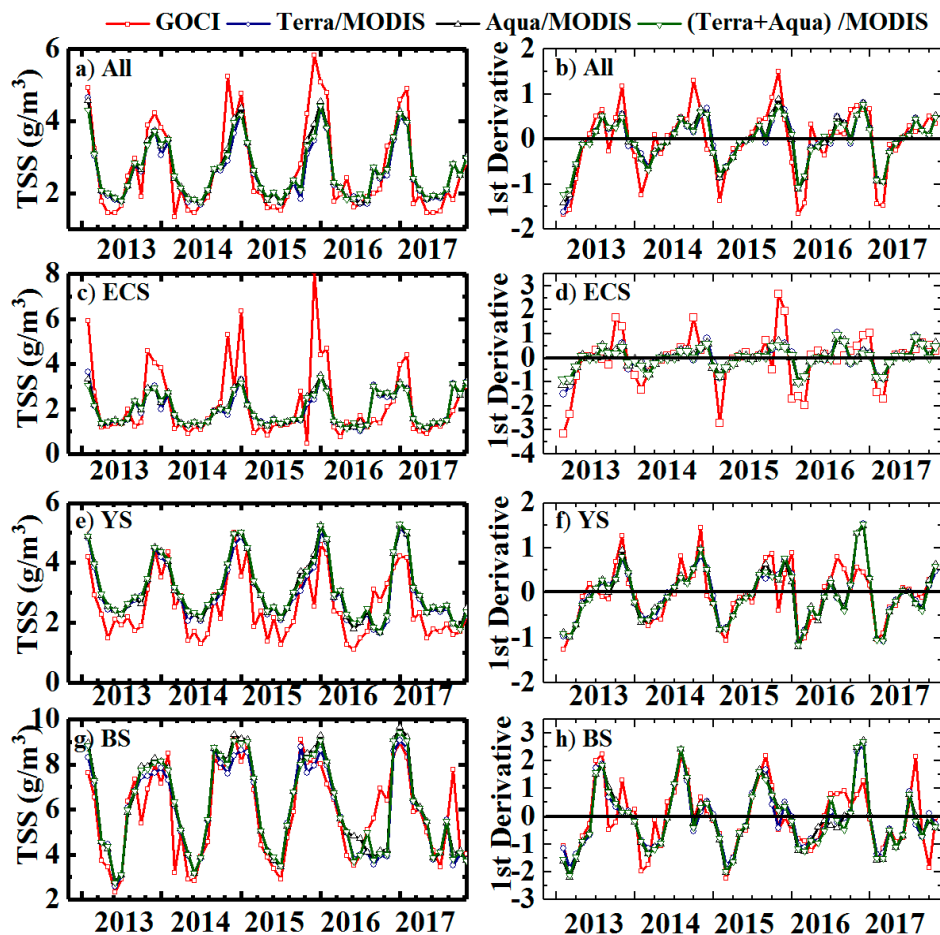


Figure 15. Monthly statistics and first derivative of TSS variations observed from GOCI, “simulated” Terra/MODIS, Aqua/MODIS and Terra + Aqua observations.

Table 4. Monthly statistics of TSS (g/m^3) variations from GOCI, “simulated” Terra, Aqua and Terra + Aqua observations.

| | | Minimum | Median | Maximum | Range | Max/Min Ratio | Missed Trends |
|-----|--------------|---------|--------|---------|-------|---------------|---------------|
| ALL | GOCI | 1.35 | 2.07 | 5.82 | 4.47 | 4.32 | - |
| | Terra | 1.69 | 2.38 | 4.65 | 2.96 | 2.76 | 8 |
| | Aqua | 1.71 | 2.41 | 4.55 | 2.84 | 2.66 | 10 |
| | Terra + Aqua | 1.77 | 2.45 | 4.42 | 2.65 | 2.80 | 10 |
| ECS | GOCI | 0.49 | 1.42 | 8.06 | 7.57 | 16.57 | - |
| | Terra | 1.00 | 1.61 | 3.65 | 2.65 | 3.65 | 13 |
| | Aqua | 1.15 | 1.64 | 3.51 | 2.35 | 3.04 | 12 |
| | Terra + Aqua | 1.10 | 1.66 | 3.42 | 2.32 | 3.71 | 11 |
| YS | GOCI | 1.10 | 2.23 | 4.99 | 3.89 | 4.54 | - |
| | Terra | 1.66 | 2.78 | 5.13 | 3.47 | 3.09 | 8 |
| | Aqua | 1.69 | 2.84 | 5.25 | 3.57 | 3.12 | 8 |
| | Terra + Aqua | 1.70 | 2.90 | 5.30 | 3.60 | 3.12 | 8 |
| BS | GOCI | 2.32 | 5.90 | 9.23 | 6.92 | 3.99 | - |
| | Terra | 2.58 | 5.86 | 9.05 | 6.47 | 3.51 | 13 |
| | Aqua | 2.80 | 5.70 | 9.66 | 6.86 | 3.45 | 10 |
| | Terra + Aqua | 2.77 | 5.80 | 9.43 | 6.65 | 3.50 | 10 |

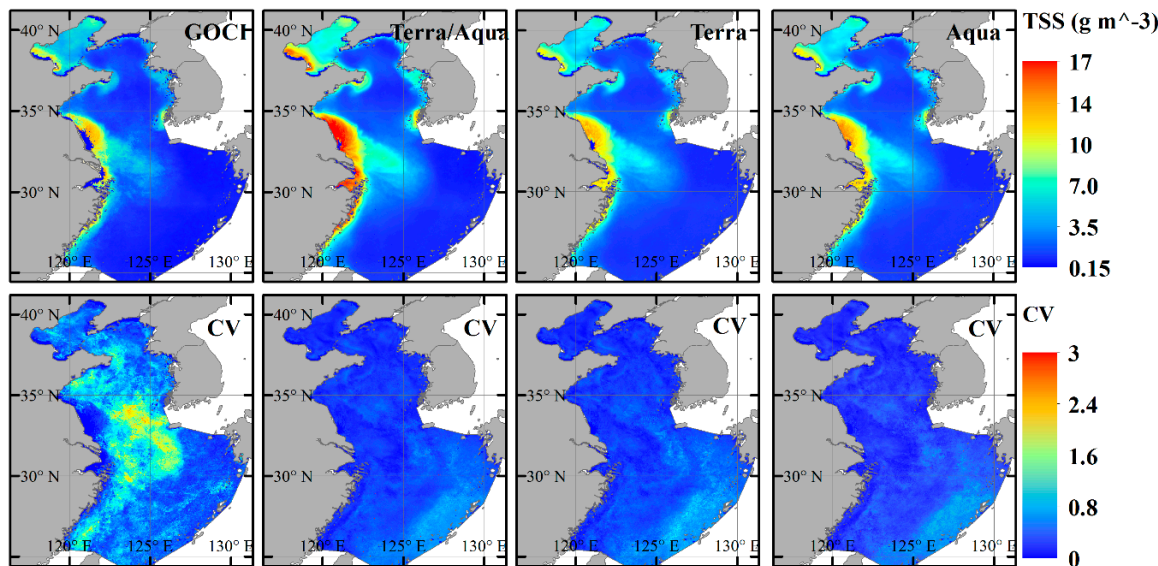


Figure 16. Annual mean TSS distributions and CV of China's seas from different sampling frequency observations from 2013 to 2017.

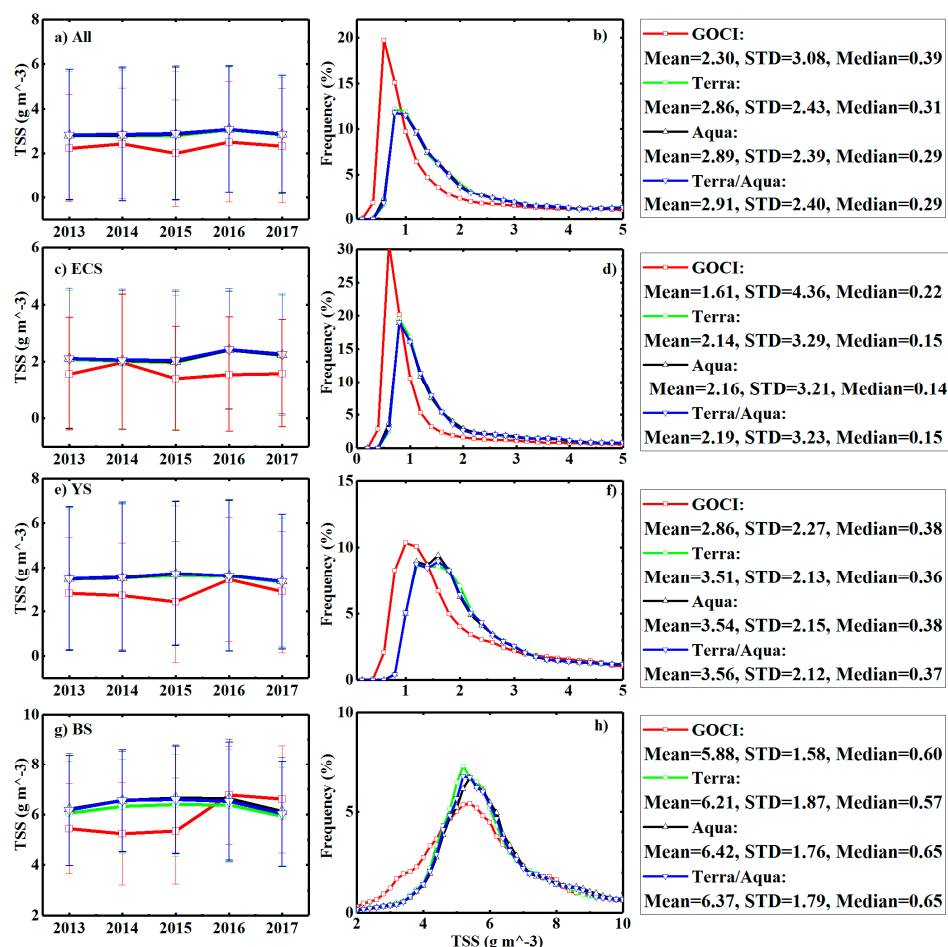


Figure 17. Annual trends and histograms of TSS (a,c,e,g) in China's seas from different sampling frequency (b,d,f,h) observations from 2013 to 2017.

Another concern when limited numbers of remote-sensing observations were applied for long-term TSS monitoring was the uncaptured tendencies of changes in the time-series, from Terra, Aqua or

Terra/Aqua MODIS, at both monthly and annual scales (Figures 16 and 17). The tendency of changes between successive months or years could be calculated by the first derivative or slope, as shown in Figure 17c-h. Differences between derivatives, from Terra, Aqua or Terra/Aqua MODIS time-series, with regard to TSS and the reference GOCI time-series suggested that the tendencies of changes might be omitted for the Terra/Aqua MODIS systems. Since reference GOCI datasets were free of the impacts of different data source, complications resulted from different calibrations, atmospheric corrections, sensitivity drifts or means of data processing. This is evidenced by Figure 15, the “missed trends” for each region of interest, as comparisons of different time-series to the GOCI reference. In general, approximately 10 monthly tendencies on average were missed in the Terra, Aqua or Terra/Aqua MODIS observations, with the maximum number of 13, and as a consequence, 16.7% of the monthly variations were not captured from 2013 to 2017. Similar results were found at the annual scale, for instance, while an increasing trend from 2013 to 2014 was revealed for the ECS in GOCI observations, a stable or slight decreasing trend was obtained in Terra/Aqua MODIS dataset. Therefore, caution should be taken when limited numbers of observations are used for the monitoring of long-term trends in the water quality parameter, a common approach in ocean color remote-sensing.

4. Discussion

4.1. Advantages of High-Frequency Observations Compared to Conventional Terra/Aqua MODIS

Ocean color sensors, such as the Terra/Aqua MODIS system, have successfully been used to monitor water quality in inland, coastal and open ocean waters. Previous studies have demonstrated that the observations are often heavily hampered by clouds, and as a result, the average valid MODIS image retrieval rate over the global oceans was only 12% per day [10,19,20]. While some research effort has been dedicated to improving the temporal coverage by merging multiple data sources, systematic assessments of the impact of cloud coverage on MODIS observations, and the knock-on effect on water quality monitoring, remains rare, and there is an outstanding requirement for more of such studies.

This study further revealed that cloud coverage for China’s seas was extremely high, for both the Terra/MODIS and Aqua/MODIS systems, with percentages of 67% and 63.2%, respectively, as listed in Table 5. Cloud coverage levels from the Terra/MODIS system were generally higher than afternoon observations from the Aqua/MODIS system, for each sub region as well as for the entire study area. The results are also consistent with previous studies on valid ocean observation rates from the Terra/Aqua MODIS systems [21]. These showed that there were more valid Aqua observations than Terra observations, due to lower cloud coverage in the afternoons.

Table 5. Cloud coverage of Terra/Aqua MODIS imagery over China’s seas, compared to GOCI observations.

| | Bohai Sea (BS) | Yellow Sea (YS) | East China Sea (ECS) | All |
|-------------|----------------|-----------------|----------------------|--------|
| Terra/MODIS | 61.80% | 74.80% | 75.10% | 67.00% |
| Aqua/MODIS | 59.20% | 67.30% | 69.70% | 63.20% |
| GOCI | 32.54% | 37.28% | 47.86% | 52.24% |

Monthly averaged data products are one of the key resources used for building time-series datasets for the analysis of ocean color parameters, including suspended sediments, chlorophyll and euphotic depth. One issue with using remote sensing data to generate high-level monthly and annually averaged datasets is that they may not reflect actual trends if there are too few valid observations [25]. The mean relative bias in monthly mean observations from the Terra/Aqua MODIS system was affected by cloud coverage. These were compared to the GOCI datasets that included eight observations per day. For the entire study area, the relative biases ranged from 9.5% to 20% for the Terra/MODIS system. For the Aqua/MODIS system, biases from 6.6% to 14.6% were revealed, with the maximum bias found

in October. Larger biases were displayed in the Terra MODIS observations than the Aqua MODIS observations, and these may have been caused by more cloud coverage, as shown above.

Cloud coverage on remote sensing images would greatly reduce valid observations, and thus introduce sampling uncertainties in short- or long-term water quality monitoring. As revealed in Section 3.2, the average biases of monthly TSS estimates were 14.1%, 7.6% and 12.2% in the ECS, BS and YS, respectively. Such results were comparable with previous studies, such as a global root mean-square error (RMSE) of 8% observed for annual mean chlorophyll concentrations, due to missing data from CZCS [18]. Barnes and Hu demonstrated that the difference between monthly mean Chl-a products for MODIS and SeaWiFS could be larger than 10% if monthly valid observations are less than 15 in the Gulf of Mexico region [27], which means the monthly sampling frequency should be larger than 50%. In a similar study conducted by Xiao Yanfang et al., a bias greater than 15% could be induced in the Yellow and East China Sea if the monthly data are averaged from 3 days, and 30% bias if the monthly data are from 1 day only [20]. However, one drawback of previous studies is that both the analysis and results were obtained using daily merged products, which means diurnal variations were missed.

Another concern when lacking effective observations is that it reduces the quality of time-series ocean color products. For instance, the monthly and annual TSS products from Terra/MODIS or Aqua/MODIS observations mostly seem to be missing the maximum and minimum values, compared to the GOCI products. The entire study region showed a range of 4.47 g/m³ when using GOCI, with maximum and minimum TSS of 1.35 and 5.52 g/m³, whereas the ranges were 2.96, 2.84 and 2.65 g/m³ from Terra, Aqua and Terra/Aqua MODIS, respectively, as shown in Figure 15 and Table 4. The benefits of high-frequency GOCI data include the improved ability to capture water quality variations more quickly, in cases a few hours before or after a large cloud/rainstorm has passed over the area and sediment is transported out into these waters. Therefore, stationary satellite remote sensing is preferred for water quality monitoring, especially in highly dynamic water regions.

4.2. Implications for Future *in situ* and Remote Sensing Sampling Strategies

Previous studies suggested that for observations of highly dynamic waters, sampling intervals of 30 min to 1 h should preferably be taken [24], and inappropriate sampling frequencies and times can lead to large biases, and could eventually lead to unscientific decisions being made during water management. A previous study has indicated that inappropriate sampling time and frequency could lead to statistical errors larger than 50% during water quality monitoring [7,25,26]. The results presented here demonstrate that while ocean color sensors, including polar-orbit satellite sensors, such as the Terra/Aqua MODIS system, are regularly used for water quality monitoring, the impacts of cloud coverage on valid observation rates and sampling biases should be taken into consideration. This is more critical when evaluating regions where the water quality undergoes more complex variations, which may be obscured by larger sampling biases. It is important to develop an optimal sampling strategy that incorporates both *in situ* and remote sensing observations, in order to minimize the effects of cloud coverage, and to obtain more valid observations or matchups for system modeling and validation of the remote sensing products.

Since geostationary ocean color satellite coverage is currently not available for most regions, and will not be for the foreseeable future, polar-orbit satellites are still the primary data source for ocean color research and applications. More polar-orbit ocean color satellite missions are currently scheduled to be launched by space agencies around the world. For instance, three ocean color missions—the Haiyang (HY) series, including the HY-1D and the HY-1E/F—are planned for launch in 2019 and 2021, respectively, by the Chinese National Space Administration (CNSA). These will contribute to surveys of the environment in China’s offshore waters, islands and coastal zones, as well as performing research on the global oceanic environment. Other missions include the PACE system from NASA in the USA, and the EnMAP from the DLR, Germany. The results of this study could, therefore, serve as a guide to avoiding cloud coverage and maximizing valid observations.

The number of hours corresponding to minimum TSS sampling biases were calculated and are shown in Figure 18 and Table 6. Notable variance was found at different spatial locations and in different months. For the entire region and the Bohai Sea, the most appropriate sampling time window ranges from 12:30 to 15:30, while this time window narrowed from 13:30 to 15:30 for observations in the East China Sea and the Yellow Sea.

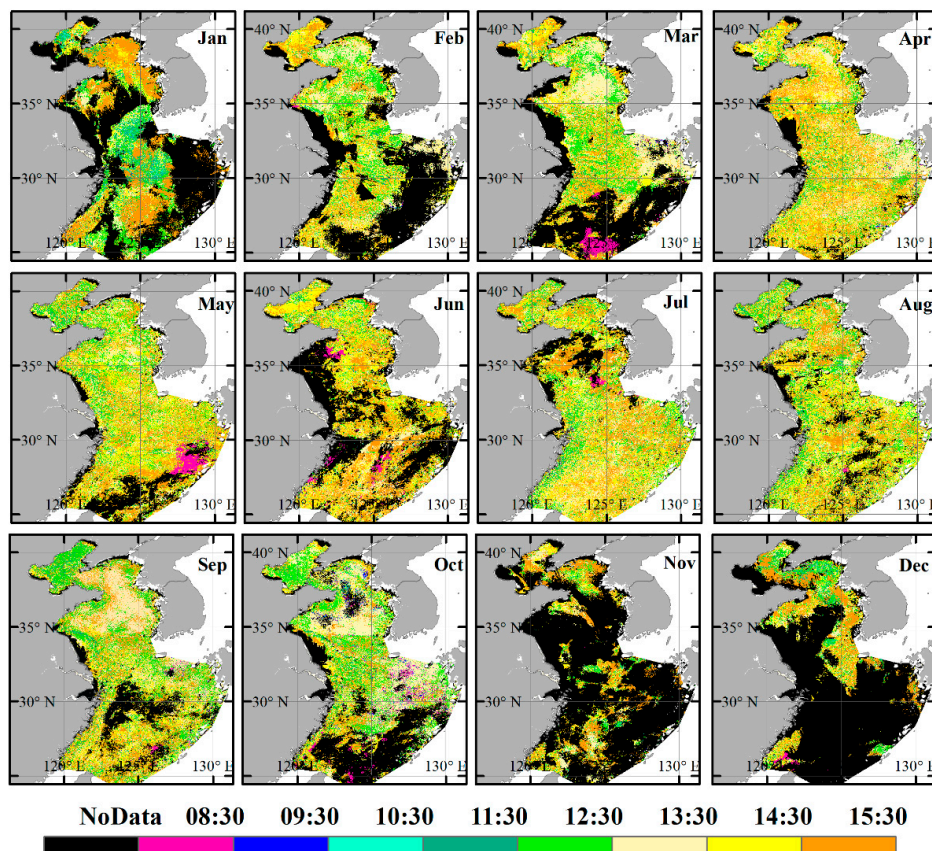


Figure 18. Hours corresponding to minimum TSS sampling bias. The results were calculated based on days with eight observations from GOCI (2013–2017). The black color denotes regions with inadequate data during calculations.

Table 6. Hours corresponding to minimum TSS sampling bias and cloud coverage for each region.

| | Hours of Minimum TSS Bias Errors | | | | Hours of Minimum Cloud Coverage | | | |
|-----|----------------------------------|-------|-------|-------|---------------------------------|-------|-------|-------|
| | All | ECS | BS | YS | All | ECS | BS | YS |
| Jan | 15:30 | 15:30 | 14:30 | 15:30 | 15:30 | 15:30 | 15:30 | 15:30 |
| Feb | 13:30 | 13:30 | 14:30 | 13:30 | 15:30 | 15:30 | 15:30 | 15:30 |
| Mar | 13:30 | 13:30 | 14:30 | 13:30 | 13:30 | 13:30 | 13:30 | 13:30 |
| Apr | 14:30 | 15:30 | 14:30 | 15:30 | 11:30 | 11:30 | 13:30 | 12:30 |
| May | 14:30 | 15:30 | 12:30 | 13:30 | 14:30 | 14:30 | 14:30 | 14:30 |
| Jun | 15:30 | 15:30 | 14:30 | 14:30 | 12:30 | 11:30 | 13:30 | 12:30 |
| Jul | 15:30 | 13:30 | 15:30 | 15:30 | 12:30 | 11:30 | 13:30 | 12:30 |
| Aug | 14:30 | 14:30 | 12:30 | 15:30 | 12:30 | 11:30 | 13:30 | 13:30 |
| Sep | 13:30 | 13:30 | 12:30 | 13:30 | 12:30 | 12:30 | 13:30 | 13:30 |
| Oct | 13:30 | 13:30 | 12:30 | 13:30 | 15:30 | 15:30 | 15:30 | 15:30 |
| Nov | 15:30 | 15:30 | 15:30 | 15:30 | 13:30 | 13:30 | 13:30 | 13:30 |
| Dec | 12:30 | 15:30 | 15:30 | 15:30 | 15:30 | 15:30 | 14:30 | 15:30 |

The sampling strategy or temporal coverage of satellite sensors is designed based on a compromise between orbital characteristics, the Field of View (FOV) or maximum scan angle [28], and cloud coverage information. The information set out in this article shows that information regarding the profiles and significance of water quality parameters, such as TSS, can also be applied to the design of future ocean color missions. This information can be used for informing scheduling studies that guide the revisit time windows, as well as for field data collection strategies, remote sensing modeling, and data product validation.

Although the results of this study are region- and sensor-dependent, it is feasible to adapt the approach to other areas in other time zones, as well as other water quality parameters, including chlorophyll, CDOM, etc. A new generation of remote sensing data is now becoming available, especially from optical remote sensors on geostationary satellites, which would provide a much higher temporal resolution—typically an image once or more per hour during daylight, compared to once per day, for instance, for the PACE system from NASA in the USA and the EnMAP from the DLR, Germany, as well as the GOCI II from Korea. These new ocean color sensors with higher temporal resolutions open up opportunities for dramatically improving the data availability, for resolving fast processes such as tidal or diurnal variability of phytoplankton or suspended particulate matter. Moreover, the results of this study will also benefit the design and application of polar-orbit ocean color satellite missions, such as China HY-1D and the HY-1E/F, planned for launch in 2019 and 2021, and Sentinel 3 OLCI, etc., which are designed to determine the time window of specific regions, or to evaluate the long-term uncertainties of ocean color products caused by insufficient sampling frequency or cloud coverage.

5. Conclusions

The benefits of ocean color remote sensing in scientific research and quantitative applications lie in their ability to provide high-resolution spatial and temporal observations of the earth's surface. This study, however, reveals that insufficient observations caused by cloud coverage have significant impacts on both the short- and long-term monitoring of ocean color parameters, especially for highly dynamic waters in coastal regions. The effects of the cloud coverage dominated at the monthly scale, with the mean normalized bias (P_{bias}) for TSS measurements of 14.1% ($\pm 2.6\%$), 7.6% ($\pm 2.3\%$) and 12.2% ($\pm 4.3\%$) in the ECS, BS and YS, respectively. Although satellite sensors, including the Terra/Aqua MODIS system, have been widely used for ocean color research and applications, uncertainties due to insufficient observations were evidently revealed for monthly and annual scale products. Evaluations of the effects of insufficient sampling observations made by the Terra/Aqua MODIS systems showed that P_{bias} ranged from 6.5% ($\pm 7.4\%$) to 20% ($\pm 13.1\%$) with the monthly scale TSS products. Much information would be missed, such as maximum values and variation ranges, when limited remote sensing data are adopted, and significant “missing trends” effects were revealed in monthly TSS variations, which means that approximately 16.7% of monthly variations were not captured by Terra/Aqua MODIS during the periods. For the entire region and the Bohai Sea, the most appropriate sampling time window ranges from 12:30 to 15:30, while this time window narrowed from 13:30 to 15:30 for observations in the East China Sea and the Yellow Sea. Caution should, therefore, be taken when using remote sensing datasets to obtain higher level processed data products, like monthly averaged values, particularly if there are an inadequate number of valid observations. The results of this research could be applied to analyze the uncertainties in ocean color remote sensing, and to determine the appropriate sampling times for collecting ocean color information, as well as providing a benchmark for future satellite sensor design and mission planning.

Author Contributions: J.L. conceived and designed the experiments; X.S. performed the experiments; L.T. and Q.X. helped to outline the manuscript structure; and Q.S. and R.T. helped to prepare the manuscript. All authors have read and agreed to the published version of the manuscript.

Funding: This work was supported by the National Key R&D Program of China (2018YFB0504900, 2018YFB0504904, 2016YFC0200900), the National Natural Science Foundation of China (Nos. 41571344, 41701379, 41331174, and 41406205), the Open Research Fund of State Key Laboratory of Simulation and Regulation of Water Cycle in River Basin, The Startup Foundation for Introducing Talent of NUISTChina Institute of Water Resources and Hydropower Research, Grant NO. IWHR-SKL-KF201809, Wuhan University Luojia Talented Young Scholar project, Dragon 4 proposal ID 32442, entitled "New Earth Observations tools for Water resource and quality monitoring in Yangtze wetlands and lakes (EOWAQYWET)", LIESMARS Special Research Funding, the "985 Project" of Wuhan University; Special funds of State Key Laboratory for equipment.

Conflicts of Interest: The authors declare no conflict of interest.

References

1. Ritchie, J.C.; Zimba, P.V.; Everitt, J.H. Remote Sensing Techniques to Assess Water Quality. *Photogramm. Eng. Remote Sens.* **2003**, *69*, 695–704. [[CrossRef](#)]
2. Wang, Y.; Xia, H.; Fu, J.; Sheng, G. Water quality change in reservoirs of shenzhen, China: Detection using landsat/tm data. *Sci. Total Environ.* **2004**, *328*, 195. [[CrossRef](#)] [[PubMed](#)]
3. Mouw, C.B.; Greb, S.; Aurin, D.; Digiocomo, P.M.; Lee, Z.; Twardowski, M.; Binding, C.; Hu, C.; Ma, R.; Moore, T.; et al. Aquatic color radiometry remote sensing of coastal and inland waters: Challenges and recommendations for future satellite missions. *Remote Sens. Environ.* **2015**, *160*, 15–30. [[CrossRef](#)]
4. Feng, L.; Hu, C.; Chen, X.; Cai, X.; Tian, L.; Gan, W. Assessment of inundation changes of Poyang Lake using MODIS observations between 2000 and 2010. *Remote Sens. Environ.* **2012**, *121*, 80–92. [[CrossRef](#)]
5. Matthews, M.W.; Bernard, S.; Robertson, L. An algorithm for detecting trophic status (chlorophyll-a), cyanobacterial-dominance, surface scums and floating vegetation in inland and coastal waters. *Remote Sens. Environ.* **2012**, *124*, 637–652. [[CrossRef](#)]
6. McClain, C.R.; Meister, G. *Mission Requirements for Future Ocean-Colour Sensors*; International Ocean-Colour Coordinating Group (IOCCG) Report Series, No. 13; IOCCG: Dartmouth, NS, Canada, 2012.
7. Zhou, Q.; Tian, L.; Wai, O.W.H.; Li, J.; Sun, Z.; Li, W. Impacts of Insufficient Observations on the Monitoring of Short- and Long-Term Suspended Solids Variations in Highly Dynamic Waters, and Implications for an Optimal Observation Strategy. *Remote Sens.* **2018**, *10*, 345. [[CrossRef](#)]
8. Gregg, W.W.; Rousseaux, C.S. Simulating PACE Global Ocean Radiances. *Front. Mar. Sci.* **2017**, *4*, 2095. [[CrossRef](#)] [[PubMed](#)]
9. Hu, C.; Feng, L.; Lee, Z.; Davis, C.O.; Mannino, A.; McClain, C.R.; Franz, B.A. Dynamic range and sensitivity requirements of satellite ocean color sensors: Learning from the past. *Appl. Opt.* **2012**, *51*, 6045–6062. [[CrossRef](#)]
10. Maritorena, S.; D'Andon, O.H.F.; Mangin, A.; Siegel, D.A. Merged satellite ocean color data products using a bio-optical model: Characteristics, benefits and issues. *Remote Sens. Environ.* **2010**, *114*, 1791–1804. [[CrossRef](#)]
11. Li, J.; Chen, X.; Tian, L.; Huang, J.; Feng, L. Improved capabilities of the Chinese high-resolution remote sensing satellite GF-1 for monitoring suspended particulate matter (SPM) in inland waters: Radiometric and spatial considerations. *ISPRS J. Photogramm. Remote Sens.* **2015**, *106*, 145–156. [[CrossRef](#)]
12. Choi, J.-K.; Park, Y.-J.; Ahn, J.-H.; Lim, H.-S.; Eom, J.; Ryu, J.-H. GOCHI, the world's first geostationary ocean color observation satellite, for the monitoring of temporal variability in coastal water turbidity. *J. Geophys. Res. Oceans* **2012**, *117*, C09004. [[CrossRef](#)]
13. Ody, A.; Doxaran, D.; Vanhellemont, Q.; Nechad, B.; Novoa, S.; Many, G.; Bourrin, F.; Verney, R.; Pairaud, I.L.; Gentili, B. Potential of High Spatial and Temporal Ocean Color Satellite Data to Study the Dynamics of Suspended Particles in a Micro-Tidal River Plume. *Remote Sens.* **2016**, *8*, 245. [[CrossRef](#)]
14. Zolfaghari, K.; Duguay, C. Estimation of Water Quality Parameters in Lake Erie from MERIS Using Linear Mixed Effect Models. *Remote Sens.* **2016**, *8*, 473. [[CrossRef](#)]
15. Joshi, I.D.; D'Sa, E.J.; Osburn, C.L.; Bianchi, T.S.; Ko, D.S.; Oviedo-Vargas, D.; Arellano, A.R.; Ward, N. Assessing chromophoric dissolved organic matter (CDOM) distribution, stocks, and fluxes in Apalachicola Bay using combined field, VIIRS ocean color, and model observations. *Remote Sens. Environ.* **2017**, *191*, 359–372. [[CrossRef](#)]
16. Concha, J.; Mannino, A.; Franz, B.; Kim, W. Uncertainties in the Geostationary Ocean Color Imager (GOCHI) Remote Sensing Reflectance for Assessing Diurnal Variability of Biogeochemical Processes. *Remote Sens.* **2019**, *11*, 295. [[CrossRef](#)]

17. Kaufman, Y.J.; Remer, L.A.; Tanre, D.; Li, R.-R.; Kleidman, R.; Mattoo, S.; Levy, R.C.; Eck, T.; Holben, B.; Ichoku, C.; et al. A critical examination of the residual cloud contamination and diurnal sampling effects on MODIS estimates of aerosol over ocean. *IEEE Trans. Geosci. Remote Sens.* **2005**, *43*, 2886–2897. [[CrossRef](#)]
18. Racault, M.-F.; Sathyendranath, S.; Platt, T. Impact of missing data on the estimation of ecological indicators from satellite ocean-colour time-series. *Remote Sens. Environ.* **2014**, *152*, 15–28. [[CrossRef](#)]
19. Gregg, W.W. *Ocean-Colour Data Merging*; International Ocean-Colour Coordinating Group: Dartmouth, NS, Canada, 2007.
20. Yanfang, X.; Jie, Z.; Tingwei, C. Analysis of the effective observation of ocean color satellites of the Yellow and East China Seas. *Remote Sens. Lett.* **2018**, *9*, 656–665. [[CrossRef](#)]
21. Feng, L.; Hu, C.; Barnes, B.B.; Mannino, A.; Heidinger, A.; Strabala, K.; Iraci, L.T. Cloud and Sun-glint statistics derived from GOES and MODIS observations over the Intra-Americas Sea for GEO-CAPE mission planning. *J. Geophys. Res. Atmos.* **2017**, *122*, 1725–1745. [[CrossRef](#)]
22. Gregg, W.W.; Woodward, R.H. Improvements in coverage frequency of ocean color: Combining data from SeaWiFS and MODIS. *IEEE Trans. Geosci. Remote Sens.* **1998**, *36*, 1350–1353. [[CrossRef](#)]
23. Feng, L.; Hu, C. Comparison of Valid Ocean Observations Between MODIS Terra and Aqua Over the Global Oceans. *IEEE Trans. Geosci. Remote Sens.* **2015**, *54*, 1575–1585. [[CrossRef](#)]
24. Antoine, D. *Ocean-Colour Observations from a Geostationary Orbit*; International Ocean-Colour Coordinating Group (IOCCG) Report Series, No. 12; IOCCG: Dartmouth, NS, Canada, 2012.
25. Gregg, W.W.; Casey, N.W. Sampling biases in MODIS and SeaWiFS ocean chlorophyll data. *Remote Sens. Environ.* **2007**, *111*, 25–35. [[CrossRef](#)]
26. Chen, Z.; Hu, C.; Muller-Karger, F.E.; Luther, M.E. Short-term variability of suspended sediment and phytoplankton in Tampa Bay, Florida: Observations from a coastal oceanographic tower and ocean color satellites. *Estuar. Coast. Shelf Sci.* **2010**, *89*, 62–72. [[CrossRef](#)]
27. Barnes, B.B.; Hu, C. Cross-Sensor Continuity of Satellite-Derived Water Clarity in the Gulf of Mexico: Insights Into Temporal Aliasing and Implications for Long-Term Water Clarity Assessment. *IEEE Trans. Geosci. Remote Sens.* **2014**, *53*, 1761–1772. [[CrossRef](#)]
28. International Ocean-Colour Coordinating Group. *Mission Requirements for Future Ocean-Colour Sensors*; IOCCG: Dartmouth, NS, Canada, 2013; Volume 13.
29. Lamquin, N.; Mazeran, C.; Doxaran, D.; Ryu, J.-H.; Park, Y.-J. Assessment of GOCI radiometric products using MERIS, MODIS and field measurements. *Ocean Sci. J.* **2012**, *47*, 287–311. [[CrossRef](#)]
30. Moon, J.-E.; Park, Y.-J.; Ryu, J.-H.; Choi, J.-K.; Ahn, J.-H.; Min, J.-E.; Son, Y.-B.; Lee, S.-J.; Han, H.-J.; Ahn, Y.-H. Initial validation of GOCI water products against in situ data collected around Korean peninsula for 2010–2011. *Ocean Sci. J.* **2012**, *47*, 261–277. [[CrossRef](#)]
31. Qiu, Z.; Zheng, L.; Zhou, Y.; Sun, D.; Wang, S.; Wu, W. Innovative GOCI algorithm to derive turbidity in highly turbid waters: A case study in the Zhejiang coastal area. *Opt. Express* **2015**, *23*, A1179–A1193. [[CrossRef](#)]
32. Kang, G.; Coste, P.; Youn, H.; Faure, F.; Choi, S. An In-Orbit Radiometric Calibration Method of the Geostationary Ocean Color Imager. *IEEE Trans. Geosci. Remote Sens.* **2010**, *48*, 4322–4328. [[CrossRef](#)]
33. Ryu, J.-H.; Han, H.-J.; Cho, S.; Park, Y.-J.; Ahn, Y.-H. Overview of geostationary ocean color imager (GOCI) and GOCI data processing system (GDPS). *Ocean Sci. J.* **2012**, *47*, 223–233. [[CrossRef](#)]
34. Qin, Y. Study of influence of sediment loads discharged from huanghe river on sedimentation in bonhai sea and huanghe sea. In Proceedings of the International Symposium on “Sedimentation on the Continental Shelf with Special Reference to the East China Sea”, Yantai, China, 16 January 1983; pp. 56–79.
35. Wang, H.; Wang, A.; Bi, N.; Zeng, X.; Xiao, H. Seasonal distribution of suspended sediment in the Bohai Sea, China. *Cont. Shelf Res.* **2014**, *90*, 17–32. [[CrossRef](#)]
36. Yang, Z.; Ji, Y.; Bi, N.; Lei, K.; Wang, H. Sediment transport off the Huanghe (Yellow River) delta and in the adjacent Bohai Sea in winter and seasonal comparison. *Estuar. Coast. Shelf Sci.* **2011**, *93*, 173–181. [[CrossRef](#)]

37. Wang, H.; Bi, N.; Saito, Y.; Wang, Y.; Sun, X.; Zhang, J.; Yang, Z. Recent changes in sediment delivery by the Huanghe (Yellow River) to the sea: Causes and environmental implications in its estuary. *J. Hydrol.* **2010**, *391*, 302–313. [[CrossRef](#)]
38. Tang, Q.; Wang, S.; Qiu, Z.; Sun, D.; Bilal, M. Variability of the Suspended Particle Cross-Sectional Area in the Bohai Sea and Yellow Sea. *Remote Sens.* **2019**, *11*, 1187. [[CrossRef](#)]
39. Bao, X.; Li, Z.; Wang, Y.; Li, N. Sediment distribution features in the north yellow sea during summer and winter. *J. Sediment Res.* **2010**, *2*, 48–56.
40. Yu, L.-L.; Jiang, W.-S. Seasonal variations in the distributions of suspended fine particulate matter in the yellow sea and the east china sea. *Oceanol. Limnol. Sin.* **2011**, *42*, 474–481.
41. Dong, L.; Guan, W.; Chen, Q.; Li, X.; Liu, X.; Zeng, X. Sediment transport in the Yellow Sea and East China Sea. *Estuar. Coast. Shelf Sci.* **2011**, *93*, 248–258. [[CrossRef](#)]
42. Liu, Z.-X.; Berné, S.; Saito, Y.; Lercolais, G.; Marsset, T. Quaternary seismic stratigraphy and paleoenvironments on the continental shelf of the East China Sea. *J. Asian Earth Sci.* **2000**, *18*, 441–452. [[CrossRef](#)]
43. Hu, C.; Feng, L.; Lee, Z. Evaluation of GOI sensitivity for At-Sensor radiance and GDPS-Retrieved chlorophyll-a products. *Ocean Sci. J.* **2012**, *47*, 279–285. [[CrossRef](#)]
44. Ahn, J.-H.; Park, Y.-J.; Kim, W.; Lee, B. Simple aerosol correction technique based on the spectral relationships of the aerosol multiple-scattering reflectances for atmospheric correction over the oceans. *Opt. Express* **2016**, *24*, 29659. [[CrossRef](#)]
45. Ahn, J.-H.; Park, Y.-J.; Ryu, J.-H.; Lee, B.; Oh, I.S. Development of atmospheric correction algorithm for Geostationary Ocean Color Imager (GOCI). *Ocean Sci. J.* **2012**, *47*, 247–259. [[CrossRef](#)]
46. Siswanto, E.; Tang, J.; Yamaguchi, H.; Ahn, Y.-H.; Ishizaka, J.; Yoo, S.; Kim, S.-W.; Kiyomoto, Y.; Yamada, K.; Chiang, C.; et al. Empirical ocean-color algorithms to retrieve chlorophyll-a, total suspended matter, and colored dissolved organic matter absorption coefficient in the Yellow and East China Seas. *J. Oceanogr.* **2011**, *67*, 627–650. [[CrossRef](#)]
47. Min, J.; Choi, J.-K.; Park, Y.; Ryu, J.H. In Retrieval of Suspended Sediment Concentration in the Coastal Waters of Yellow Sea from Geostationary Ocean Color Imager (goci). In Proceedings of the International Symposium on Remote Sensing, Chiba, Japan, 10 May 2013; pp. 15–17.
48. Ruddick, K.G.; Vanhellemont, Q.; Yan, J.; Neukermans, G.; Wei, G.; Shang, S. Variability of suspended particulate matter in the Bohai Sea from the geostationary Ocean Color Imager (GOI). *Ocean Sci. J.* **2012**, *47*, 331–345. [[CrossRef](#)]
49. Choi, J.-K.; Yang, H.; Han, H.-J.; Ryu, J.-H.; Park, Y.-J. Quantitative estimation of suspended sediment movements in coastal region using GOI. *J. Coast. Res.* **2013**, *165*, 1367–1372. [[CrossRef](#)]
50. Wang, M.; Ahn, J.-H.; Jiang, L.; Shi, W.; Son, S.; Park, Y.-J.; Ryu, J.-H. Ocean color products from the Korean Geostationary Ocean Color Imager (GOI). *Opt. Express* **2013**, *21*, 3835–3849. [[CrossRef](#)] [[PubMed](#)]
51. Son, S.; Kim, Y.-H.; Kwon, J.-I.; Kim, H.-C.; Park, K.-S. Characterization of spatial and temporal variation of suspended sediments in the Yellow and East China Seas using satellite ocean color data. *GISci. Remote Sens.* **2014**, *51*, 212–226. [[CrossRef](#)]
52. Park, Y.J.; Ahn, Y.H.; Han, H.; Yang, H.; Moon, J.; Ahn, J.; Lee, B.; Min, J.; Lee, S.; Kim, K.; et al. Goci Level 2 Ocean Color Products Brief Algorithm Description. Available online: http://kosc.kiost.ac.kr/download.php?fileName=ATBD_master_v9_1.pdf (accessed on 12 April 2015).
53. Lee, H.J.; Park, J.Y.; Lee, S.H.; Lee, J.M.; Kim, T.K. Suspended Sediment Transport in a Rock-Bound, Macrotidal Estuary: Han Estuary, Eastern Yellow Sea. *J. Coast. Res.* **2013**, *29*, 358–371. [[CrossRef](#)]
54. Wang, W.; Jiang, W. Study on the seasonal variation of the suspended sediment distribution and transportation in the East China Seas based on SeaWiFS data. *J. Ocean Univ. China* **2008**, *7*, 385–392. [[CrossRef](#)]
55. Chen, J.; Liu, J. The spatial and temporal changes of chlorophyll-a and suspended matter in the eastern coastal zones of china during 1997–2013. *Cont. Shelf Res.* **2015**, *95*, 89–98. [[CrossRef](#)]
56. Bian, C.; Jiang, W.; Quan, Q.; Wang, T.; Greatbatch, R.J.; Li, W. Distributions of suspended sediment concentration in the Yellow Sea and the East China Sea based on field surveys during the four seasons of 2011. *J. Mar. Syst.* **2013**, *121*, 24–35. [[CrossRef](#)]

57. Yuan, D.; Zhu, J.; Li, C.; Hu, D. Cross-shelf circulation in the Yellow and East China Seas indicated by MODIS satellite observations. *J. Mar. Syst.* **2008**, *70*, 134–149. [[CrossRef](#)]
58. He, X.; Bai, Y.; Pan, D.; Huang, N.; Dong, X.; Chen, J.; Chen, C.-T.A.; Cui, Q. Using geostationary satellite ocean color data to map the diurnal dynamics of suspended particulate matter in coastal waters. *Remote Sens. Environ.* **2013**, *133*, 225–239. [[CrossRef](#)]



© 2020 by the authors. Licensee MDPI, Basel, Switzerland. This article is an open access article distributed under the terms and conditions of the Creative Commons Attribution (CC BY) license (<http://creativecommons.org/licenses/by/4.0/>).